International Journal of Mechanical Sciences 87 (2014) 200–217

Contents lists available at ScienceDirect

International Journal of Mechanical Sciences

journal homepage: www.elsevier.com/locate/ijmecsci

Effect of the cube orientation on formability for FCC materials: A detailed comparison between full-constraint and self-consistent predictions

M.A. Bertinetti [b], C.D. Schwindt [c], J.W. Signorelli [a,b,*]

[a] IFIR (CONICET), 27 de Febrero 210 bis, 2000 Rosario, Argentina
[b] FCEIA (UNR), Pellegrini 250, 2000 Rosario, Argentina
[c] Department of Engineering, UNS-CONICET, Alem 1253, 8000 Bahía Blanca, Argentina

ARTICLE INFO

Article history:
Received 20 October 2013
Received in revised form
16 April 2014
Accepted 30 May 2014
Available online 7 June 2014

Keywords:
Forming-limit diagrams
MK-VPSC
Orientation stability
Geometrical hardening

ABSTRACT

A rate-dependent self-consistent (VPSC) polycrystal-plasticity model, in conjunction with the MK approach, has been used successfully to address and explain plastic deformation features and localization conditions that cannot be treated with the full-constraint (FC) Taylor scheme. Signorelli and Bertinetti [On the role of constitutive model in the forming limit of FCC sheet metal with cube orientations, *International Journal of Mechanical Sciences*, 51: 473–480, 2009] investigated FCC sheet-metal formability, focusing on how the cube texture affects localized necking. In the present work, we extent this research to include two types of textures experimentally observed in aluminum alloys: the {100} ⟨001⟩ Cube orientation rotated 45° with respect to the sheet normal direction; and the {100} ⟨uvw⟩ orientations. The effect of these orientations on the FLD is studied numerically, and a detailed comparison between MK-FC and MK-VPSC, derived from orientation stability and geometrical hardening, is made. The classical MK model, based on strain-rate imposed boundary conditions, was generalized in order to explicitly and correctly includes stress boundary conditions for materials with changes in anisotropy during deformation. In plane-strain stretching, the enhanced formability of the rotated 45° {100} ⟨001⟩ orientations has been correlated with texture evolution. In equi-biaxial stretching, the MK-FC approach predicted greater limit-strain values than did the MK-VPSC model. Qualitative differences in geometrical hardening/softening were also found.

1. Introduction

Most sheet metals employed in stretch forming operations are produced by a combination of rolling and annealing. As a consequence, typical preferred orientations are inevitably present in rolled sheets. These orientations cannot be completely transformed into an entirely random state by annealing. Investigation of the behavior of these orientations contributes to a deeper understanding of material deformation mechanisms, microstructural evolution and mechanical anisotropy. It is widely recognized that crystallographic textures strongly affect the formability of polycrystalline sheet metals. In rolled FCC sheets, crystallographic textures are frequently classified in terms of the ideal rolling and recrystallization components. FCC materials can show many different recrystallization textures, even for similar alloys having the same deformation texture, as was underlined in the review of Grewen and Huber [1]. For example, Duckham et al. [2] analyzed the evidence that precipitate nucleation at shear bands leads to a randomization of the recrystallization texture in a 1 wt% Mg commercial-purity aluminum alloy and studied how this material's texture is related to the accumulated deformation and temperature. They founded that there is a remarkable increase in the Cube volume fraction (from 30 to 40%) as the deformation temperature increases from 300 to 350°C, with a corresponding decrease in the random component. Crumbach et al. [3] studied three aluminum alloys, cold rolled to different thickness reductions and annealed at different temperatures. They pointed out that the final textures differed substantially, but all were typical of recrystallized aluminum alloys. These deformation textures contained not only the Cube component but also the {001} ⟨uvw⟩ (ND-Cube) orientations. Because aluminum alloys generally exhibit less ductility than might be desired (less than steel alloys for example), increasing their formability by controlling the texture remains highly relevant.

Many researchers have investigated, experimentally and computationally, the influence of different starting textures and work-hardening behavior on the deformation of aluminum sheets,

* Corresponding author at: IFIR (CONICET), 27 de Febrero 210 bis, 2000 Rosario, Argentina. Tel.: +54 341 480 8545; fax: +54 341 482 1772.
E-mail address: signorelli@ifir-conicet.gov.ar (J.W. Signorelli).

http://dx.doi.org/10.1016/j.ijmecsci.2014.05.031
0020-7403/

including the development of material anisotropy. Among others, Choi et al. [4] studied the macroscopic anisotropy of AA5019A sheets, containing the typical texture components of the H48 and O temper conditions. The cold-rolled material (AA5019A-H48) has a strong rolling texture and weak Cube component, while the AA5019A-O sheet contains a strong Cube and minimal rolling texture components. Their experimental investigation included tensile tests to measure yield stresses and plastic–strain ratios, and they combined these results with predictions of plastic properties performed with both Taylor (FC) and viscoplastic self-consistent (VPSC) models. They concluded that the FC model not only underestimated r-values, particularly for loading at 45° to the rolling direction, but incorrectly predicted the orientational dependence of yield stress. To the contrary, the VPSC simulations were in good agreement with the experimental results. Lopes et al. [5] extensively studied a recrystallized, strongly Cube textured AA1050-O sheet in order to gain insight on how crystallographic texture affects strain-hardening anisotropy in proportional tensile loading. In their research, the authors deformed tensile specimens oriented at 0°, 45° and 90° to the rolling direction (RD), measuring the stress–strain behavior. They observed that the 45° orientation exhibited much higher strain hardening, and as a result, had greater uniform elongations, 30% and 25% more than the 0° and 90° specimens respectively. Similarly, the measured strain-rate sensitivity exponent, m, at 45° was higher than that in the transverse direction (TD). They suggested that post-uniform elongation ductility could be higher for 45° tension, making this direction very resistant to plastic-flow localization. Later, Yoon et al. [6] investigated the same AA1050-O alloy, confirming a preponderant {100} ⟨001⟩ Cube texture in the {111} pole figure for the as-received material. They also observed that the strain hardening was higher at 45° than in the rolling and transverse directions. Recently, Chiba et al. [7] used the Marciniak test technique to measure an AA1100-H24 sheet's forming-limit strains. This information was then used to verify the phenomenological Yld2000-2d and FC Taylor-type crystal-plasticity models. Both mechanical properties and measured texture data provided input to calibrate the models. They found that both models had limitations in the prediction of the measured limit strains.

Recently, Yanaga et al. [8] performed biaxial tensile tests of aluminum alloy sheets with different Cube-orientation intensities, which they referred to as High Cube (HC) and Low Cube (LC) textures. They found greater through-thickness thinning at the top of a bulged LC textured sheet –with respected to the HC material – and the opposite at the periphery, near the die profile, explaining this in terms of the differences in the shapes of the HC and LC work contours. Plane-strain elongation at the periphery was accelerated in the case of the HC material, producing the greater reduction in thickness. They determined that the difference in HC and LC crystallographic texture produced different flow-stress relations between equi-biaxial tension and plane-strain tension, in the two sheets. The observed uniaxial responses along 0°, 45° and 90° were consistent with the higher ductility of the Cube-type material at 45° to the rolling direction.

Within a computational framework, Wu et al. [9] analyzed forming limits for a family of Cube textures that had orientations spreading around the ideal {001} ⟨001⟩. They found, unexpectedly, that near biaxial stretching the calculated forming-limit diagrams (FLDs) are significantly higher for texture dispersions of 11° and 15° around the ideal Cube orientation than for a random texture. Yoshida et al. [10] made the same observation, finding that it is only the Cube-texture component that produces this result. Moreover, they reported that the forming-limit curve for a Cube texture is significantly increased when the sheet is stretched along the 45° (R-Cube) direction relative to the rolling direction. This effect is pronounced near plane-strain forming paths. Such a result is in agreement with the work reported by Yanaga et al. [8] for a higher hardening exponent at 45° than at 0° and 90° in the case of a High Cube textured 6061-T4 aluminum alloy sheet. Nevertheless, Yoshida and co-workers found that the predicted limit-strain drops drastically in uniaxial stretching for an ideal R-Cube texture with a Gaussian spread of 15°. Subsequently, Yoshida et al. [11] showed that the {001} ⟨uvw⟩ (ND-Cube) texture enhances the forming-limit curve for the full range of linear strain paths. They concluded that, for a general stamping operation, the {001} ⟨uvw⟩ texture is highly advantageous because of its high formability irrespective of blank's orientation. However, the authors note that these results are entirely computational, based on the polycrystal–plasticity model. They also acknowledge that both the strain hardening and forming limit have not been observed experimentally for the strong Cube textured and/or rotated Cube textured aluminum alloy sheets. These sheets were numerically subjected to plane-strain and equi-biaxial stretching modes. It is important to mention that all calculations performed by Wu and by Yoshida were based on a generalized FC Taylor-type polycrystal model in conjunction with the Marciniak–Kuczynski (MK) instability analysis [12]. Signorelli and Bertinetti [13] revisited the Cube-texture results discussed by Wu et al. [9], but used a VPSC formulation plus the MK approach. The simulations carried out within this framework gave qualitatively different results than the MK-FC approach when limit strains were calculated from the ideal Cube orientation through various dispersions to the random texture. The MK-VPSC approach predicted a smooth transition in the calculated failure strains. Also, these MK-VPSC calculations predicted that a random texture would give the greatest biaxial formability, as expected. These results demonstrate that the constitutive model selected is critically important for predicting the behavior of materials that evolve anisotropically during mechanical deformation. More recently, Yoshida and Kuroda [14] simulated plastic-deformation characteristics and stretchability of textured aluminum alloy sheets using a crystal-plasticity model. They reexamined the influence of texture and r-value on stretchability and concluded that the material's capacity to strain-harden in plane-strain deformation is a key factor in producing superior formability over the entire biaxial-stretching range.

The present contribution complements our previous work [13], that investigated the role of the constitutive relation in modeling the forming limit of FCC sheet metal with Cube orientations, including R-Cube and ND-Cube type materials. This study focuses on evaluating the relation between orientation stability and geometrical hardening, and determining how this relationship affects the forming-limit strain, particularly near the plane-strain and balanced-biaxial stretching modes. Additionally, the classical MK model, based on strain-rate imposed boundary conditions, was generalized in order to explicitly and correctly include stress boundary conditions for materials with changes in anisotropy during deformation.

The paper is organized as follows. First, a brief review of the basic equations and definitions for MK and VPSC theories are presented, together with a description of the formulation used to model necking. The predicted FLDs for the different Cube-type textures are evaluated. Because it is known that the Cube and R-Cube orientations are not stable for particular applications, this theoretical study was performed using an orientation stability analysis. Finally, we discuss the geometrical hardening/softening effects predicted by the FC and VPSC models and how they affect the limit-strain behavior. Results show that, in the plane-strain mode, the observed limit-strain behavior is in agreement with the predicted geometrical hardening. To the contrary, in equi-biaxial tension, the FC model indicates there is a geometrical hardening contribution to the flow stress, while a softening trend is predicted by VPSC.

2. Theoretical framework

We begin this section with the basic kinematic definitions of crystal-plasticity theory. The kinematic development of a single-crystal plasticity model has been well documented by several authors e.g. Kocks et al. [15], Roters et al. [16]. Here we assume that, during plastic-forming operations, it is possible to neglect the elastic contribution to deformation. Consequently, we will restrict ourselves to a rate-dependent plastic response at the single-crystal level.

2.1. Viscoplastic crystal plasticity

The total deformation of a crystal is mainly the result of two mechanisms: dislocation motion within the active slip systems and lattice distortion [17]. A multiplicative decomposition of the deformation-gradient tensor $\mathbf{F}$ can be used to take these two aspects into account:

$$\mathbf{F} = \mathbf{F}^e.\mathbf{F}^p \tag{1}$$

where $\mathbf{F}^p$ and $\mathbf{F}^e$ are the plastic and elastic contributions, which account for the accumulative effect of dislocation motion and the remaining non-plastic deformation, respectively [18]. We assume that essentially $\mathbf{F}^p$ leaves the crystal lattice not only undistorted, but also unrotated. Thus, the distortion and rotation of the lattice is only contained in $\mathbf{F}^e$, such that $\mathbf{F}^e = \mathbf{R}$, and the crystallographic rotation matrix $\mathbf{R}$ is specified in terms of the three Euler angles $(\varphi_1, \phi, \varphi_2)$ – Bunge convention – as

$$\mathbf{R} = \begin{bmatrix} \cos\varphi_1 \cos\varphi_2 - \sin\varphi_1 \sin\varphi_2 \cos\phi & \sin\varphi_1 \cos\varphi_2 + \cos\varphi_1 \sin\varphi_2 \cos\phi & \sin\varphi_2 \sin\phi \\ -\cos\varphi_1 \sin\varphi_2 - \sin\varphi_1 \cos\varphi_2 \cos\phi & -\sin\varphi_1 \sin\varphi_2 + \cos\varphi_1 \cos\varphi_2 \cos\phi & \cos\varphi_2 \sin\phi \\ \sin\varphi_1 \sin\phi & -\cos\varphi_1 \sin\phi & \cos\phi \end{bmatrix} \tag{2}$$

By including this consideration in Eq. (1), the velocity-gradient tensor can be written as

$$\mathbf{L} = \dot{\mathbf{F}}.\mathbf{F}^{-1} = \dot{\mathbf{R}}.\mathbf{R}^{\mathbf{T}} + \mathbf{R}.\mathbf{L}^{\boldsymbol{p}}.\mathbf{R}^{\mathbf{T}} \tag{3}$$

where $\mathbf{L}^p = \dot{\mathbf{F}}^p.\mathbf{F}^{p-1}$ is the plastic velocity-gradient. The tensor $\mathbf{L}^p$ can be determined from dislocation motion along specific planes and directions in the crystal

$$\mathbf{L}^p = \sum_s \mathbf{n}^s \otimes \mathbf{b}^s \dot{\gamma}^s \tag{4}$$

here $\mathbf{b}^s$ is the slip plane direction or Burgers' vector, $\mathbf{n}^s$ is the slip plane normal direction and $\dot{\gamma}^s$ is the accumulative shear strain, which determines the crystal reorientation. The Schmid orientation tensor, defined as $\mathbf{n}^s \otimes \mathbf{b}^s$, has symmetric $\mathbf{m}^s$ and skew-symmetric $\mathbf{q}^s$ components given by

$$\mathbf{m}^s = \frac{1}{2}(\mathbf{n}^s \otimes \mathbf{b}^s + \mathbf{b}^s \otimes \mathbf{n}^s), \tag{5}$$

$$\mathbf{q}^s = \frac{1}{2}(\mathbf{n}^s \otimes \mathbf{b}^s - \mathbf{b}^s \otimes \mathbf{n}^s). \tag{6}$$

To describe the plastic behavior of a single crystal, a constitutive viscoplastic model written in terms of each slip system is postulated. Particularly, in the present work, we adopt a viscoplastic potential law [19] expressed as

$$\dot{\gamma}^s = \dot{\gamma}_0 \left|\frac{\tau_r^s}{\tau_c^s}\right|^{1/m} \operatorname{sign}(\tau_r^s) = \dot{\gamma}_0 \left|\frac{\mathbf{m}^s : \mathbf{S}}{\tau_c^s}\right|^{1/m} \operatorname{sign}(\mathbf{m}^s : \mathbf{S}) \tag{7}$$

where $\dot{\gamma}_0$ is the reference shear rate, τ_r^s is the resolved shear stress on slip system s, τ_c^s is the critical resolved shear stress (CRSS), $\mathbf{S}$ is the deviatoric stress tensor and m is the strain-rate sensitivity exponent which is typically taken to be quite small (on the order of ~0.02) to represent rate independent cases. When the crystal is subjected to stresses, slip activates when the shear stress reaches the critical value $\tau_r^s = \tau_c^s$ on any system.

The local viscoplastic constitutive relation between the strain-rate and the deviatoric stress, can be written in a pseudo-linear form, defining a single-crystal, viscoplastic secant modulus, $\mathbf{M}$:

$$\mathbf{D} = \dot{\gamma}_0 \sum_s \frac{\mathbf{m}^s \otimes \mathbf{m}^s}{\tau_c^s} \left|\frac{\mathbf{m}^s : \mathbf{S}}{\tau_c^s}\right|^{1/(m-1)} : \mathbf{S} = \mathbf{M} : \mathbf{S} \tag{8}$$

In the present study, an anisotropic hardening scheme accounts for the strain hardening between slip systems, and the evolution of the critical shear stresses can be expressed in the following general form:

$$\dot{\tau}_c = \sum_s h^s |\dot{\gamma}^s| \tag{9}$$

where h^s are the hardening-moduli behaviors, which depend on γ, the accumulated sum of the single slip contributions γ^s. These moduli can be written using the initial hardening rate, h_0, and the hardening exponent n, arranged in the following power-law form:

$$h^s = h_0 \left(\frac{h_0 \gamma}{\tau_c^s n} + 1\right)^{n-1} \tag{10}$$

$$\gamma = \sum_s \int_0^t |\dot{\gamma}^s| \, dt$$

2.1.1. Taylor – full constraint model (FC)

The classical Taylor model assumes that the ensemble of grains in the polycrystal deforms homogeneously, fulfilling the compatibility condition [15]. The imposed external macroscopic strain corresponds to the internal microscopic strain. Additionally, the overall strain rate, deviatoric stress and viscoplastic compliance are determined from the corresponding magnitudes at the grain level as follows:

$$\begin{aligned} \overline{\mathbf{D}} &= \mathbf{D}, \\ \overline{\mathbf{S}} &= \langle \mathbf{S} \rangle \\ \overline{\mathbf{M}} &= \langle \mathbf{M}^{-1} \rangle^{-1} \end{aligned} \tag{11}$$

where $\langle\,\rangle$ and $\overline{}$ denote a weighted average over all grains in the polycrystal and the corresponding magnitude at the aggregate level, respectively. Typically the set of discrete orientations, that characterize the material texture, could be obtained from the recalculated ODF. Local deviatoric stress states could be evaluated by solving Eq. (8).

2.1.2. Viscoplastic self-consistent model (VPSC)

Contrary to the FC model, the self-consistent approach represents each grain as an ellipsoidal viscoplastic inhomogeneity embedded in and interacting with a homogeneous effective medium (HEM). This approach fully accounts for the grain's anisotropic properties. As initially proposed by Molinari et al. [20] and Lebensohn and Tomé [21], the VPSC model allows each grain to deform differently, according to its directional properties and the strength of the interaction between the grain and its surroundings. If a stress or deformation rate is applied to the outer

boundary of the HEM, the inhomogeneity induces local deviations of the stress and the strain rate in its vicinity. When the local response of the medium is linear, the interaction between the grain and the HEM is solved using the Eshelby inclusion formalism [22]. The properties of the HEM are not known a priori, and are adjusted self-consistently to coincide with the average of all the grains in the aggregate. Here, we outline the relevant concepts and equations of the VPSC model. For a full description of the formulation, the reader is referred to the original paper [21]. The VPSC approach is characterized by an interaction equation relating the strain rate and deviatoric stress in each grain ($\mathbf{D}$, $\mathbf{S}$) to the averages over the polycrystal ($\overline{\mathbf{D}}$,$\overline{\mathbf{S}}$). This is done through the interaction tensor $\tilde{\mathbf{M}}$

$$\mathbf{D}-\overline{\mathbf{D}}=-\tilde{\mathbf{M}}(\mathbf{S}-\overline{\mathbf{S}}), \tag{12}$$

which is a function of the overall modulus and the shape and orientation of the ellipsoid that represents the embedded grain. Details concerning the self-consistent equations can be found in [15] and [21]. The macroscopic (overall) secant modulus $\overline{\mathbf{M}}$ can be adjusted iteratively using the following self-consistent equation:

$$\overline{\mathbf{M}}=\langle \mathbf{M}:(\mathbf{M}+\tilde{\mathbf{M}})^{-1}:(\overline{\mathbf{M}}+\tilde{\mathbf{M}})\rangle \tag{13}$$

with $\overline{\mathbf{D}}=\overline{\mathbf{M}}:\overline{\mathbf{S}}$.

2.1.3. Texture evolution

After convergence in each strain increment is obtained, the crystallographic orientation of each grain must be updated according to the total lattice rotation-rates (lattice spin) $\dot{\boldsymbol{\Omega}}$. Taking the sample system frame as a reference, $\dot{\boldsymbol{\Omega}}$ are given as follows:

$$\dot{\boldsymbol{\Omega}}_{\mathbf{FC}}=\overline{\mathbf{W}}-\sum_s \mathbf{q}^s\dot{\gamma}^s \tag{14a}$$

$$\dot{\boldsymbol{\Omega}}_{\mathbf{SC}}=\overline{\mathbf{W}}-\sum_s \mathbf{q}^s\dot{\gamma}^s+\tilde{\mathbf{W}} \tag{14b}$$

where $\overline{\mathbf{W}}$ is the skew-symmetric part of the prescribed velocity gradient $\overline{\mathbf{L}}$. For the case of self-consistent model, the tensor $\tilde{\mathbf{W}}$ describes the additional rotation-rate deviation in the ellipsoidal domain, associated with the skew-symmetric part of the Eshelby tensor and the local strain-rate deviation in the grain.

2.2. Necking analysis

The FLD simulations were conducted using the well-known MK analysis. It is known that elasticity affects the initiation of material localization, especially near the necking region and it cannot be neglected in any local description. However, based on the previous works, taking elasticity into account in the MK framework does not appreciably modify the predicted limit-strain profiles, allowing for the use of a rigid-plastic constitutive description. For example, Wu et al. [23] examined the effect of crystal elasticity on the FLD finding only a slightly overestimation of formability with a 100 fold increase in the elastic modulus. More recently, Wang et al. [24], using an elastic-viscoplastic self-consistent model and the MK approach, found that the choice of elastic modulus does not affect the predicted FLD value by more than 0.5% under monotonic loadings. In what follows, we outline the principal details of the MK model together with a skeletal framework of its numerical implementation in conjunction with the VPSC model. In the extended approach, developed by Hutchinson and Neale [25], strain localization occurs due to the existence of a material imperfection or a local heterogeneity, such as a groove or a narrow band across the width of the sheet, which is initially inclined at an angle Ψ_0 with respect to the principal axis (Fig. 1). As the homogeneous zone is proportionally strained in the MK model, the groove grows continuously to finally result in a localized neck.

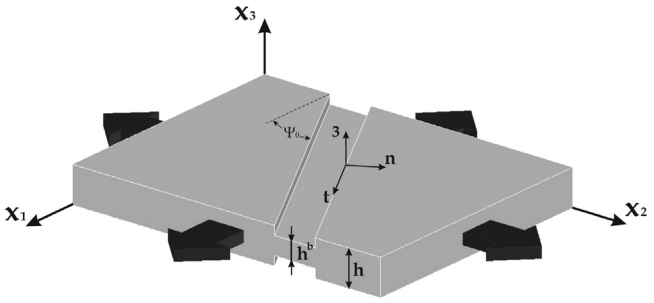

Fig. 1. MK geometry.

Tensor components are expressed with respect to the global cartesian x_i coordinate system. A second set of axes referenced to the band is used in the model, with the normal and tangential directions of the band defining the axes in the sheet plane. The 3 direction is taken normal to the sheet itself ($\mathbf{n}$,$\mathbf{t}$,$\mathbf{3}$). Quantities inside the band are denoted by the subscript b.

The initial imperfection factor f_0 is characterized by an initial thickness ratio inside and outside the band

$$f_0=\frac{h_b(0)}{h(0)} \tag{15}$$

here $h_b(0)$ and $h(0)$ are the initial thickness in the band and in the homogeneous zone, respectively.

The velocity gradient outside the band has the following form:

$$\overline{\mathbf{L}}=\overline{L}_{11}\begin{bmatrix}1 & 0 & 0\\ 0 & \rho & 0\\ 0 & 0 & -(1+\rho)\end{bmatrix} \tag{16}$$

where the imposed strain path on the edges of the sheet is assumed as

$$\rho=\frac{\overline{L}_{22}}{\overline{L}_{11}}=\frac{\overline{D}_{22}}{\overline{D}_{11}}=\text{const.} \tag{17}$$

$$\overline{\mathbf{L}}^b=\overline{\mathbf{L}}+\dot{\mathbf{c}}\otimes\mathbf{n} \tag{18}$$

Eq. (18) is decomposed into the symmetric strain rate tensor, $\overline{\mathbf{D}}^b$, and the skew-symmetric tensor of rigid-body rotation rate, $\overline{\mathbf{W}}^b$

$$\overline{\mathbf{D}}^b=\overline{\mathbf{D}}+\frac{1}{2}(\dot{\mathbf{c}}\otimes\mathbf{n}+\mathbf{n}\otimes\dot{\mathbf{c}}),$$
$$\overline{\mathbf{W}}^b=\overline{\mathbf{W}}+\frac{1}{2}(\dot{\mathbf{c}}\otimes\mathbf{n}-\mathbf{n}\otimes\dot{\mathbf{c}}) \tag{19}$$

here, $\mathbf{n}$ is the unit normal to the band, and $\dot{\mathbf{c}}$ is a vector to be determined. The equilibrium conditions required at the band interface are given by

$$\mathbf{n}\,\overline{\boldsymbol{\sigma}}^b\,h_b=\mathbf{n}\,\overline{\boldsymbol{\sigma}}\,h \tag{20}$$

where $\overline{\boldsymbol{\sigma}}$ denotes the Cauchy stress. Noting that δ_{ij} is the Kronecker symbol, the boundary condition $\overline{\sigma}_{33}=0$ is applied as follows

$$\overline{\sigma}_{ij}=\overline{S}_{ij}-\overline{S}_{33}\,\delta_{ij}\,(i=1,\,2,\,3) \tag{21}$$

The integration of the polycrystalline model inside and outside the band is performed as follows. First, an increment of strain is applied to the material in the homogeneous zone, $\overline{\mathbf{D}}\Delta t$. Both inside and outside the band, it is assumed that $\overline{D}_{13}=\overline{D}_{23}=\overline{W}_{13}=\overline{W}_{23}=0$. The equilibrium condition, Eq. (20), can be expressed in the coordinate system referenced to the groove

$$\overline{\sigma}^{\mathrm{b}}_{nn}h_{\mathrm{b}}=\overline{\sigma}_{nn}h$$

$$\overline{\sigma}^{b}_{nt} h_b = \overline{\sigma}_{nt} h \tag{22}$$

The compatibility condition requires equality of elongation in the direction **t**,

$$\overline{D}^{b}_{tt} = \overline{D}_{tt} \tag{23}$$

Note that within the band, the screw component of the velocity gradient $\overline{\mathbf{W}}^{b}$ is non-zero, so the angle of the groove changes as deformation proceeds. Following Hutchinson and Neale [25] and Wu et al. [26], the evolution of the groove orientation is given by:

$$\tan\ \Psi = \exp[(1-\rho)\varepsilon_{11}]\ tan\Psi_0 \tag{24}$$

Because we are considering thin sheets with the orthotropic symmetries in the plane of the sheet, in-plane stretching produces a plane-stress state. As discussed by Kuroda and Tveergard [27], when an orthotropic material is loaded along directions not aligned with the axes of orthotropy, it is necessary to compute the $\overline{L}_{12}$ component by assuming that $\overline{\sigma}_{12}=0$. But if the axes are along the loading directions, it is the same as imposing either of the conditions $\overline{L}_{12}=0$ or $\overline{\sigma}_{12}=0$. For the general case, the unit normal vector **n** of the band is calculated by the form

$$\mathbf{n} = \frac{1}{\sqrt{t_1^2+t_2^2}} \begin{pmatrix} -F_{11}t_1^0 & -F_{12}t_2^0 \\ F_{21}t_1^0 & F_{22}t_2^0 \end{pmatrix} \tag{25}$$

Eq. (24) is a particular case of Eq. (25).

Most numerical implementations of the MK model include the resolution of non-linear systems of equations in order to determine the mechanical state in the groove zone. We proceeded in the same way in previous wors [13,28,29]. Most recently, Serenelli et al. [30] and Signorelli et al. [31] used another strategy. Their method solves the constitutive model under a mixed boundary condition, in order to determine the groove state. Using that approach we proceed as follows: the remaining unknowns $\overline{L}^{b}_{nn} = \overline{D}^{b}_{nn}$, $\overline{L}^{b}_{nt} = \overline{D}_{nt} + \overline{W}^{b}_{nt}$, $\overline{L}^{b}_{tn} = \overline{D}_{nt} - \overline{W}^{b}_{nt}$, and $\overline{L}^{b}_{33}$, $\overline{\sigma}^{b}_{tt}$, $\overline{\sigma}^{b}_{n3}$, $\overline{\sigma}^{b}_{t3}$ can be evaluated directly, after solving for the state $(\overline{\mathbf{L}}, \overline{\boldsymbol{\sigma}})$ in the homogeneous zone and expressing the tensors in the band reference frame, together with Eqs. (22) and (23). This lets us avoid solving a nonlinear system with logic time benefits and a reduction of convergence problems. It is important to note that the mixed boundary-condition in the band reference frame is solved inside the constitutive model.

The entire FLD of a sheet is determined by repeating the procedure for different strain paths that were defined in terms of the strain-rate ratios over the range $-0.5 \le \rho \le 1$ with a step of 0.1. Since all in-plane directions are potential necking directions, a conservative estimate of the forming-limit strain is obtained by repeating the calculations for every 5 degrees of Ψ_0. If the material is loaded along directions aligned with the fixed coordinate directions ($\Theta = 0^\circ$ or 90°), we consider the values of Ψ_0 to range from 0° to 90°, and from -90° to 90° for the cases where Θ has a value other than 0° or 90°. The failure strains ε^*_{11}, ε^*_{22} outside the band and the critical failure angle Ψ^* are obtained after minimizing the curve ε^*_{11} versus Ψ_0. The sheet realizes necking when a considerably higher strain rate occurs inside the band than within the homogeneous zone. Several criteria can be defined in order to stop the incremental procedure. In the present work, failure is reached when $|\overline{D}^{b}_{33}| > 20|\overline{D}_{33}|$. We consider the numerical factor 20 large enough to verify that values close to the actual limit-strains are obtained (the numerical value of this factor is related to the magnitude of the imposed strain increment, typically in the range of 10^{-3} to 10^{-4}). The numerical algorithm of the MK-VPSC code is summarized in Fig. 2. It is important to remark that with the proposed numerical strategy it is possible to parallelize the band solutions.

The MK approach predicts the FLD based on the growth of the initial imperfection f_0. However, the strength of the imperfection

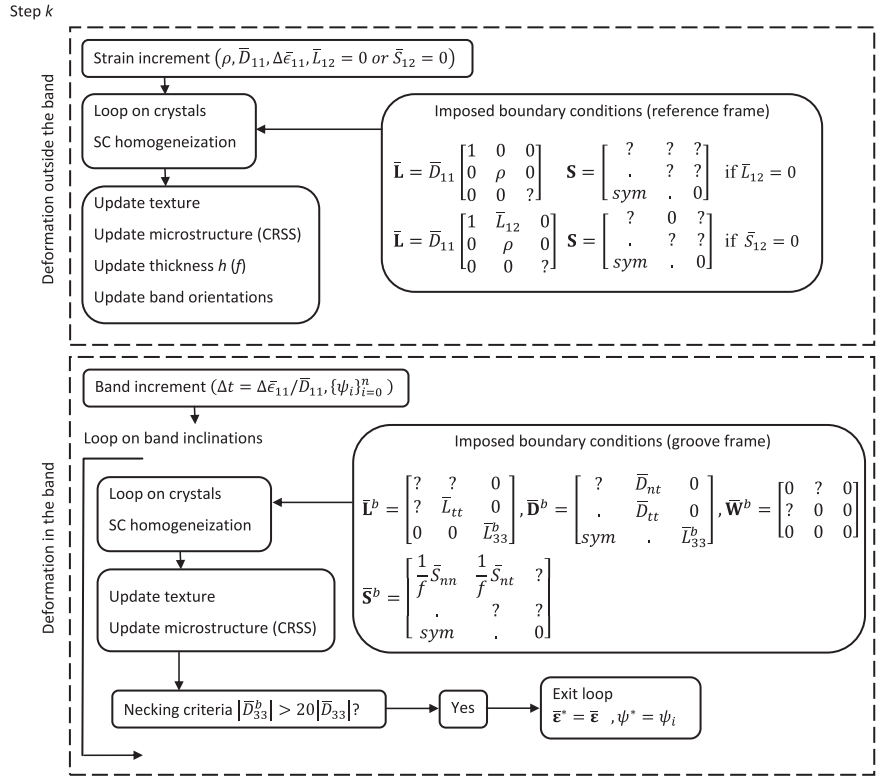

Fig. 2. Scheme of the structure of constitutive equations implemented in the MK-VPSC FLD code. Boundary conditions are explicitly shown for both zones.

cannot be directly measured by physical experiments, since this factor does not have a direct correlation with the imperfections observed in real materials. Therefore, in most of the MK model applications, f_0 is calibrated by matching the experimental FLD_0 (FLD_0 is the limit strain for the in-plane, plane-strain tension, loading condition). The value of f_0 may vary significantly, with numbers commonly found in the literature ranging between 0.98 and 0.9999. Many authors have analytically predicted the effect of the initial imperfection parameter on the FLD and demonstrated, as expected, that the forming limit strain decreases with increasing depths of the initial imperfection [26,28,32]. In general, though this factor has an important influence on the magnitude of the limit-strain values, only minor effects can be seen in the limit-strain profiles.

2.3. Stability and rotation fields analysis

In this section, we follow the work of Tóth et al. [33] to provide a short description of the basic tenets of orientation stability analysis. Each orientation is defined in Euler space by three angles $\varphi_1, \phi, \varphi_2$. Texture evolution means that orientations move during plastic deformation in orientation space, and the orientation change of a given grain can be described by the rotation field, as shown in Clement and Coulomb [34]:

$$\begin{aligned}\dot{\varphi}_1 &= \dot{\Omega}_{21} - \dot{\varphi}_2 \cos\phi \\ \dot{\phi} &= \dot{\Omega}_{32}\cos\varphi_1 + \dot{\Omega}_{13}\sin\varphi_1 \\ \dot{\varphi}_2 &= (\dot{\Omega}_{32}\sin\varphi_1 - \dot{\Omega}_{13}\cos\varphi_1)/\sin\phi\end{aligned} \tag{26}$$

One of the conditions for either convergence or divergence of a given orientation can be expressed by the divergence of the rotation field $\dot{\varphi}_1, \dot{\phi}, \dot{\varphi}_2$

$$div\dot{g} = \frac{\partial\dot{\varphi}_1}{\partial\varphi_1} + \frac{\partial\dot{\phi}}{\partial\phi} + \frac{\partial\dot{\varphi}_2}{\partial\varphi_2} \tag{27}$$

The condition $div\dot{g} < 0$ and $div\dot{g} > 0$ indicates convergence or divergence, respectively. An orientation can remain stable only if the lattice-rotation rate vanishes and the rotation field in Euler space is such that it converges on that point. An orientation is predicted metastable if the lattice-rotation rate vanishes but $div\dot{g}$ is positive. When the lattice-rotation rate is not null and $div\dot{g}$ is positive, this orientation is predicted as unstable.

These stability conditions determine whether or not the density of this orientation increases during deformation. To characterize the degree to which the orientation of an individual grain will persist, a second parameter related to the stability of an orientation can be examined through the persistence value, P, given by

$$P\left(\dot{\varphi}_1, \dot{\phi}, \dot{\varphi}_2, D_{eq}\right) = \ln\left(\frac{D_{eq}}{\dot{\varphi}_1^2 + \dot{\phi}^2 + \dot{\varphi}_2^2 + 2\dot{\varphi}_1\dot{\varphi}_2^2\cos\phi}\right) = \ln\left(\frac{D_{eq}}{\|\dot{\Omega}\|}\right) \tag{28}$$

where D_{eq} is the von Mises equivalent strain-rate. The dependency of P on $\cos\phi$ is a direct consequence of the non-Euclidian metric of the Euler space [35]. The application of this expression is not valid over the entire range of angles, since this parameter can be infinity when $\dot{\varphi}_1, \dot{\phi}, \dot{\varphi}_2$ are null or, equivalently, when $\dot{\boldsymbol{\Omega}} = 0$. Arzaghi et al. [36] overcame this difficulty proposing a sort of normalization of the lattice spin in the whole of Euler space using the maximum value of $\|\dot{\Omega}\|$. Later, Pandey et al. [37] modified the stability parameter as follows:

$$P = \ln\left(\frac{D_{eq}}{\|\dot{\boldsymbol{\Omega}}\| + D_{eq}/e^{P_{max}}}\right) \tag{29}$$

The value $P_{max}=1$ in Eq. (29) was selected so that P can vary between 0 and 1. The advantage of this equation is that it can never lead to singularities. This scalar parameter assumes the highest value in regions of Euler space where the orientation persists over large strains, and the lowest value where the degree of persistence is almost null.

3. Results and discussion

3.1. Forming-limit diagrams for the Cube, R-Cube and ND-Cube orientations

For the purpose of investigating how the typical recrystallization textures affect formability, we selected three different textures that are observed in aluminum sheets after certain deformation processes. These textures were modeled by spreading the grain orientations around the ideal Cube {100} ⟨001⟩, the ideal {100} ⟨001⟩ rotated 45° with respect to the normal direction and the {100} ⟨uvw⟩ orientations (the Cube texture rotated about the ND). These discrete orientations were reoriented in such a way that a Gaussian distribution results. The procedure for generating textures is the same as used in previous work [13]. For example, the "Cube texture" is one where the first standard deviation of grains lies within 15° of the ideal Cube {100} ⟨001⟩. In this case, it should be noted that 2/3 of the grains are inside of 15° from the ideal orientation and 1/3 of the grains are outside of it. The number of individual orientations was set in order to obtain an adequate representation of the orthotropic symmetries of a rolled sheet. Fig. 3 shows the {111} stereographic pole figures for the Cube, R-Cube and ND-Cube distributions, where 6000 discretized orientations were used to create the set of textures.

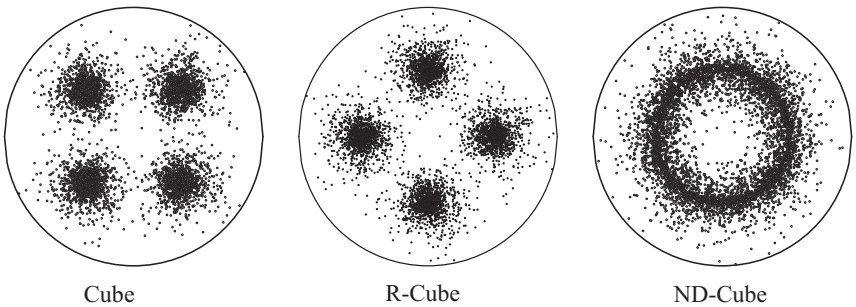

Fig. 3. Generated {111} pole figures with 6000 orientations using a Gaussian distribution with a standard deviation of 15°.

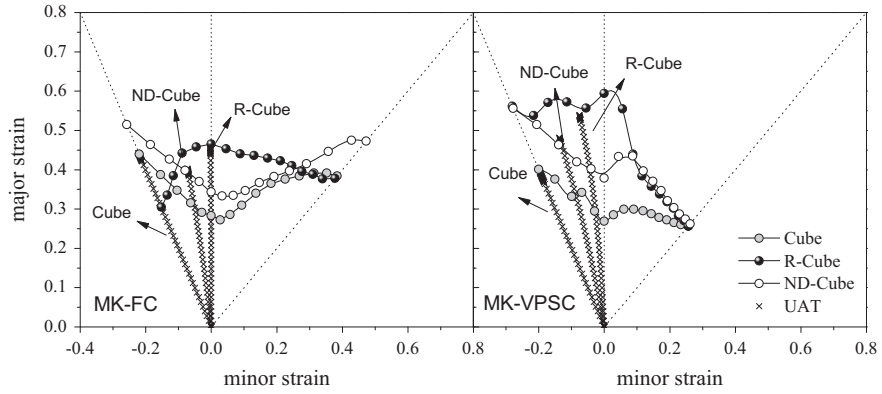

Fig. 4. Calculated FLDs assuming a Gaussian distribution with a standard deviation of 15°. Scattered-lines correspond to uniaxial tension strain paths.

In the following FLD simulations, in both the homogeneous zone and defect band, standard FCC {111} ⟨110⟩ crystallographic slip is used, and the initial textures are assumed to be the same. The material parameters are taken from Signorelli and Bertinetti [13], and are fixed at $m=0.02$, $n=0.24$, $h_0=1218$ MPa and $\tau_0=42$ MPa. The slip-induced hardening law is isotropic for all slip systems, and the reference plastic shearing rate for slip is $\dot{\gamma}_0=0.001\ s^{-1}$.We took the initial ratio of the thickness inside the band to that outside the band, f_0, to be 0.99 for all computations. Fig. 4 shows the predicted FLDs for the set of texture distributions using both MK-FC and MK-VPSC models. Results are similar but not equal to those reported by Yoshida et al. [10,11] when the MK-FC approach is used. Differences appear due to the different parameter values employed in our simulations (curves are identical when calculations are carried out with the set of parameters employed by these authors). The results clearly illustrate the differences between both homogenization schemes, particularly in tensile and biaxial stretching, although the tendency is close for the plane-strain mode ($\rho=0$). In negative strain space ($\rho<0$) both models predict similar shapes and levels for the Cube and ND-Cube set of orientations, although the calculated values for the VPSC simulations are slightly greater for ND-Cube and slightly less for Cube. The behavior is quite different for the R-Cube texture, since the FC's predicted curve slopes downwards from plane-strain to a tensile-stretching state with the minimum limit-strain value at $\rho=-0.5$. These values are far below those calculated for the two other textures. This loss of formability, also predicted by Yoshida et al. [11], does not appear when the MK-VPSC scheme is used. To the contrary, the R-Cube texture exhibits an enhanced formability, and the limit-strain values are still higher than those determined from the other two textures, except at $\rho=-0.5$ where the strain value is similar to that of the ND-Cube. For the plane-strain mode, no qualitative differences are found between approaches, though the VPSC overestimates the limit-strain values for the R-Cube, producing a major limit strain 1.3 times greater than that calculated with the FC model. On the biaxial side of the FLD, shapes and values are quite different. As we move towards balanced-biaxial loading, the FLDs approach each other and a certain matching is observed for the three textures, particularly for the VPSC calculations. For the FC case, the limit-strain values for Cube and R-Cube are identical, while values for the ND-Cube are definitely higher than the other two, again in agreement with Yoshida's results.

Normally, the FLD is simulated by imposing strain-rate boundary conditions, which in some cases restricts a direct comparison with experimental limit-strain data from formability tests, where the sheet is subjected to stress-loading conditions. This limitation is produced by the variation of r-values with straining, which follows from the material's crystallographic texture-evolution. Eq. (16) describes the boundary condition imposed on the homogeneous zone within the MK framework. The formulation can be generalized in order to explicitly include stress boundary conditions corresponding to different stress ratios, characterized by $\alpha=\overline{\sigma}_{22}/\overline{\sigma}_{11}$

$$\overline{\mathbf{L}}=\begin{bmatrix}\overline{L}_{11} & 0 & 0\\ 0 & \overline{L}_{22} & 0\\ 0 & 0 & \overline{L}_{33}\end{bmatrix},\quad \overline{\boldsymbol{\sigma}}=\begin{bmatrix}1 & 0 & 0\\ 0 & \alpha & 0\\ 0 & 0 & 0\end{bmatrix}\overline{\sigma}_{11} \tag{30}$$

The velocity-gradient tensor component $\overline{L}_{33}$ is adjusted in order to nullify the corresponding stress component. The stress ratio values $\alpha=-1$, $\alpha=0$ and $\alpha=1$, correspond to pure shear, uniaxial and biaxial test conditions, respectively. In order to contrast the predictions with experimental data from the literature, Fig. 4 includes the limit-strains predicted by both MK-FC and MK-VPSC models assuming uniaxial tension (UAT) boundary conditions ($\alpha=0$) for the Cube, R-Cube and ND-Cube material textures. Calculations carried out with the MK-FC model show that the limit strains for the R-Cube texture are slightly higher than for Cube and ND-Cube textures. The MK-VPSC values show a greater formability for R-Cube than for Cube texture. This effect is closely related to the significant change of R-Cube texture as deformation proceeds. By imposing uniaxial loading, the different strain paths mandated by the three textures are directly associated with the materials' r-values (Table 1) along the tensile direction, i.e., r_0 values. The smaller this parameter is, as in the case of R-Cube and ND-Cube textures, the smaller the width strain, leading to a shift of the strain path into the plane-strain mode. This is critical for the R-Cube texture when the FC model is used, where uniaxial tension conditions lead to a plane-strain deformation mode. These results are in agreement with the flow stress curves reported by Lopes et al. [5] and Li and Bate [38] for AA1050-O tested in the RD and TD directions, and for tensile tests performed at 45° to the RD. Particularly, Li and Bate reported that the 45° tensile samples

Table 1
Predicted r-values at 0°, 45° and 90° to the rolling direction, calculated at 20% macroscopic true strain with the FC and VPSC models.

r-Values	Cube		R-Cube		ND-Cube	
	FC	VPSC	FC	VPSC	FC	VPSC
r_0	1	1	0	0.09	0.18	0.31
r_{45}	0	0.09	1.02	1	0.16	0.28
r_{90}	1.04	1.01	0	0.09	0.18	0.30
$\bar{r}=(r_0+2r_{45}+r_{90})/4$	0.51	0.55	0.51	0.55	0.17	0.29

elongated about 25–30% more than RD and TD uniaxial tension specimens. Moreover, heat-treated aluminum alloys (AA6063 and AA7030) with typical recrystallization textures, Cube (15°) 21.6%, (100)-fiber (15°) 65.5% and Cube (15°) 48%, (100)-fiber (15°) 81.3% respectively exhibit their highest ductility at angles of between 30° and 60° to the rolling direction [39]. The predicted limit strains for Cube and R-Cube under uniaxial tension are in close agreement with the ductility (max elongation) observed in AA7030, including the reported r-value at 45° ($r_{45}=0.18$). These differences in the limit behavior under uniaxial tension loading are not well predicted by the Taylor based MK model. Other related results are listed in Table 2 [5,38–42]. To the contrary, the validation of limit-strain predictions in biaxial stretching is difficult. Contributions of Lademo et al. [42] (AA7030 cold rolled annealed 350 °C 1 min), Velmanirajan et al. [43] (AA8081 annealed 350 °C) and Pedersen et al. [44] (AA6063 extruded and recrystallized) are examples of FLD measurements for materials with different and non-negligible volume fractions of initial Cube orientations. As we will see in the following paragraph, these results show a profile closer to that observed in the FLDs when a 50% fraction of random orientations are added to the ideal condition that is displated in Fig. 4. We attribute this fact to the effect that the non-Cube orientations have on the yield surface, and consequently, on the limit behavior under biaxial stretching. The capability of our model to satisfactory predict the yield surface of HC and LC materials discussed in Yanaga et. al [8] is shown in a supplementary attachment.

The effect of orientation spread about {100} ⟨001⟩ on forming limit diagrams was studied previously [13]. In what follows, the FLDs are calculated for three texture dispersions (7°, 11° and 15°) around the ideal {100} ⟨011⟩ and {100} ⟨uvw⟩ orientations. Fig. 5 shows the calculated limit strains for the {100} ⟨011⟩ ideal orientation using MK-FC (left) and MK-VPSC (right) models. In the negative minor-strain range, as the spread decreases, VPSC tends to replicate the formability behavior predicted by FC. This is expected. Here, the smaller the spread is, the lower the limit-strain value. The correlation with textural spread is the opposite in plane strain. In this case, the highest limit-strain value is for the 7° spread. In biaxial stretching and within the MK-FC framework, the profiles of the R-Cube (11°) and R-Cube (15°) simulations are very close, while R-Cube (7°) exhibits a degraded formability as deformation approaches the balanced tensile-stretching state. MK-VPSC's limit-strain values also decrease with increasing biaxial tension. Although, all these values are lower than for the FC approach. A comparison between models shows that the MK-VPSC and MK-FC models behave and change similarly with respect to the textural dispersion. In uniaxial tension the greater the dispersion the greater the formability; in plane strain this reverses, and in balanced-biaxial tension the trend returns.

Fig. 6 shows FLDs for the ND-Cube orientations when the different spreads are considered. The predicted trends of the limit strains are similar for the left-hand side of the FLD, irrespective of whether the MK-FC or MK-VPSC model was used in the calculation. These results are also independent of the amount of orientation spread assumed. However, results are clearly different in the biaxial-stretching region, with the differences between models increasing continuously to a maximum in balanced-biaxial loading. MK-FC calculations are very close over the complete range of loading conditions, and we found no significant differences in the predictions, regardless of the selected spread. To the contrary, MK-VPSC limit strains depend significantly on ρ. The forming-limit curves slope downwards from plane-strain to equi-biaxial stretching, and over the whole range $\rho > 0$, the formability progressively

Table 2
Reported max. elongation for uniaxial true stress-strain curves at 0°, 45°, and 90° to the rolling direction for some heat-treated aluminum alloys.

Material	Obs.	Max elongation					
AA 1050-O [5]	Annealed at 343 °C 45 min (Strong Cube texture). Reported $r_{45}=0.20$	RD	0.24	DD	0.34	TD	0.26
AA1100 [38]	Hot and cold rolled (25 mm to 1 mm), annealed at 440 °C at a rate of 48° per hour	RD	0.23	DD	0.29	TD	0.22
AA6063 and AA7030 [39]	AA6063 recrystallized (Cube 21.6%, Goss 26.2% – (100)-fiber 65.5%). Reported $r_{45}=0.40$	RD	0.16	DD	0.30	TD	0.27
	AA7030 recrystallized (Cube 48.0%, Goss 7.8% – (100) fibers 81.3%). Reported $r_{45}=0.18$	RD	0.13	DD	0.32	TD	0.23
AA2024-T3 [40]	Heat treatment at 525 °C age-hardening 10^4seg. Crystallographic texture presents Cube,	Thickness (1.27 mm)					
	Goss and S ideal orientations (vol. fractions are not reported)	RD	0.22	DD	0.26	TD	0.19
		Thickness (2.03 mm)					
		RD	0.24	DD	0.26	TD	0.15
AA7075-O [41]	Cold rolled (7.2 mm to 2.1 mm), annealed at 450°C	RD	0.16	DD	0.22	TD	0.18
AA7108 and AA7030 [42]	AA7108 cold rolled at strain of 0.7, annealed at 400 °C 5 min. (Strong β-fiber)	RD	0.11	DD	0.27	TD	0.23
	AA7030 cold rolled at strain of 0.7, annealed at 350 °C 1 min. (Strong Cube texture)	RD	0.16	DD	0.22	TD	0.16

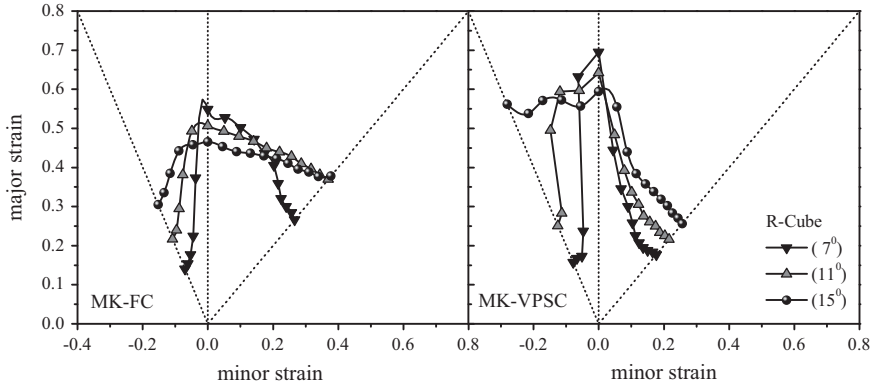

Fig. 5. Calculated FLDs for the R-Cube texture assuming the Gaussian distribution with different standard deviations.

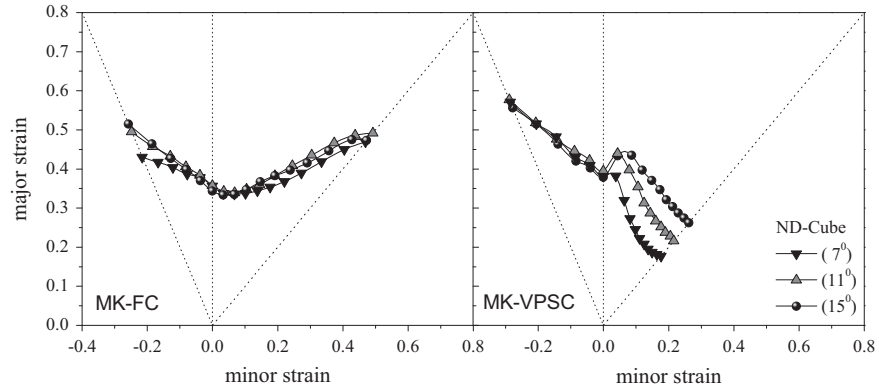

Fig. 6. Calculated FLDs for the ND-Cube texture assuming the Gaussian distribution with different standard deviations.

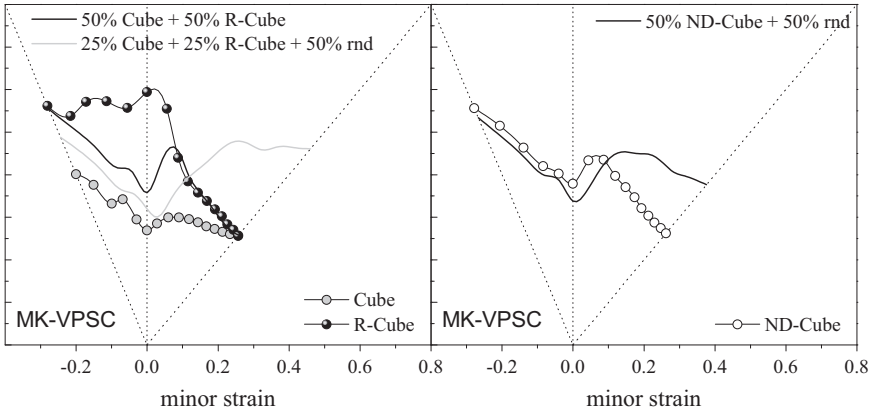

Fig. 7. Calculated FLDs for the different ideal components with the addition of random orientations. (left) Cube and R-Cube, (right) ND-Cube.

decreases with decreasing cut-off angles (a sharper distribution). It is interesting to note the possibility of a simple correlation between the limit-strain profiles of the different ideal components and the expected limit behavior for a given textured material, even though it is not the focus of the present paper. Fig. 7 (left) shows the results of a simulation performed on an equal part Cube (15°) and R-Cube (15°) ideal orientation texture. Furthermore, the effect of the orientation distribution severity was included by smoothing the material texture through the addition of 50% more grains with random orientations. The predicted limit-strain profiles reveal that it is not possible to analyze the behavior of the whole material as a simple and direct blend of individual contributions, at least for this type of ideal orientation. The enhanced formability associated with the R-Cube texture under plane-strain conditions is rapidly degraded by the presence of the Cube-type orientations. However, under uniaxial tension and particularly for biaxial stretching, the predicted limit strains are similar to that of the R-Cube. It is observed that the predicted final texture is close to that obtained for Cube and R-Cube materials under biaxial stretching. The addition of a set of random orientations decreases slightly the limit strains on the left-hand side of the FLD, while on the right-hand side the profile exhibits less pronounce variations as the balanced-biaxial condition is achieved [29]. Similar considerations can be taken for the case of a mixed texture with ND-Cube orientations (Fig. 7 right).

Several authors [5,6,11] observed enhanced formability for strong Cube-textured aluminum sheets, when they were subjected to uniaxial tension at 45° to the rolling direction. However, there is still not enough experimental limit-strain and strain-hardening data available for R-Cube and ND-Cube textured materials for us to verify the models' calibration and predictions in plane-strain and equi-biaxial stretching modes.

3.2. Stability and rotation fields around Cube and R-Cube orientations

To examine the stability of the ideal Cube and R-Cube orientations, during plane-strain and equi-biaxial stretching, the rotation rates, their gradients and divergences were calculated using the FC and the VPSC schemes. The degeneracy which arises at $\phi = 0°$ is avoided by taking one of the symmetric equivalents of the Cube and R-Cube orientations defined by the Euler angles $\varphi_1 = 0°$, $\phi = 90°$, $\varphi_2 = 90°$ and $\varphi_1 = 45°$, $\phi = 90°$, $\varphi_2 = 90°$, respectively. The quantities that involve a derivative with respect to the angular values were evaluated through finite differences in the Euler space. The full characteristics of the rotation field around a given orientation were calculated in the initial state as well as at the end of the simulation just before reaching the limit-strain. Numerical results are presented in Tables 3 and 4, for Cube and R-Cube respectively.

The calculated values for the ideal Cube orientation in plane-strain, at an initial state of deformation, were verified with those reported by Zhou and Neale [45]. It is seen from Table 3 that there is a little or no change of the rotation rates ($\dot{\varphi}_1$,$\dot{\phi}$, $\dot{\varphi}_2$) during plane-strain and equi-biaxial stretching for the FC case; one of the three terms in the divergence expression is positive, one is zero and the other is negative for $\rho = 0$, while one is zero and the others are positive for $\rho = 1$. This implies that, during plane-strain, orientations rotate towards Cube along the direction of the φ_1 axis, but move away along the ϕ axis. However, for balanced-biaxial loading, there is a two-dimensional divergence of rotation, and orientations move away along the ϕ and φ_2 axes. The changes of φ_2 are rather small in the plane-strain condition. Under the VPSC scheme the same tendency is observed, but the calculated values for the gradients are much larger than those of FC, implying

Table 3
Orientation rate, gradient, divergence and persistence of the ideal Cube orientation in plane-strain ($L_{11}=1$, $L_{22}=0$, $L_{33}=-1$) and balanced-biaxial ($L_{11}=1$, $L_{22}=1$, $L_{33}=-2$) loading calculated with the FC and VPSC models.

	FC				VPSC[a]			
	initial		close to failure		initial		close to failure	
	$\rho=0$	$\rho=1$	$\rho=0$	$\rho=1$	$\rho=0$	$\rho=1$	$\rho=0$	$\rho=1$
φ_1	0.00	0.00	0.00	0.00	0.00	0.00	0.06	0.00
ϕ	90.00	90.00	90.00	89.99	90.00	90.00	90.21	90.08
φ_2	90.00	90.00	90.00	89.86	90.00	90.00	89.99	89.35
$\dot{\varphi}_1$	0.00	0.00	0.00	0.00	0.01	0.00	0.00	0.00
$\dot{\phi}$	0.00	0.00	0.01	0.00	0.01	0.00	0.02	0.03
$\dot{\varphi}_2$	0.00	−0.01	0.00	−0.01	0.00	0.11	0.00	−0.20
$\partial\dot{\varphi}_1/\partial\varphi_1$	−1.00	0.00	−1.00	0.00	−2.53	0.00	−3.31	−0.01
$\partial\dot{\phi}/\partial\phi$	1.00	3.00	1.00	3.00	2.41	9.38	2.83	13.74
$\partial\dot{\varphi}_2/\partial\varphi_2$	0.00	3.00	0.00	3.00	0.00	9.36	−1.11	14.38
$div\dot{g}$	0.00	6.00	0.00	5.99	−0.12	18.66	−1.58	28.11
P	1.00	0.99	1.00	0.98	0.97	0.81	0.95	0.71

[a] A Gaussian distribution of 15 degrees was assumed as the HEM.

Table 4
Orientation rate, gradient, divergence and persistence of the ideal R-Cube orientation in plane-strain ($L_{11}=1$, $L_{22}=0$, $L_{33}=-1$) and balanced-biaxial ($L_{11}=1$, $L_{22}=1$, $L_{33}=-2$) loading calculated with the FC and VPSC models.

	FC				VPSC[a]			
	initial		close to failure		initial		close to failure	
	$\rho=0$	$\rho=1$	$\rho=0$	$\rho=1$	$\rho=0$	$\rho=1$	$\rho=0$	$\rho=1$
φ_1	45.00	45.00	44.97	45.00	45.00	45.00	[b]41.52	45.00
ϕ	90.00	90.00	90.02	90.01	90.00	90.00	70.16	90.12
φ_2	90.00	90.00	90.08	89.86	90.00	90.00	110.98	89.35
$\dot{\varphi}_1$	0.00	0.00	−0.01	0.00	0.00	0.00	−0.18	0.00
$\dot{\phi}$	0.01	0.00	−0.02	0.01	−0.01	0.00	−0.42	0.04
$\dot{\varphi}_2$	0.00	−0.01	0.02	−0.01	0.01	0.00	0.52	−0.19
$\partial\dot{\varphi}_1/\partial\varphi_1$	1.00	0.00	1.00	0.00	3.49	0.00	1.83	−0.01
$\partial\dot{\phi}/\partial\phi$	2.50	2.98	2.49	3.00	7.02	9.52	−5.85	15.04
$\partial\dot{\varphi}_2/\partial\varphi_2$	2.50	3.02	2.50	3.00	7.02	9.46	−6.30	13.34
$div\dot{g}$	5.99	5.99	5.99	5.99	17.53	18.98	−10.32	28.37
P	0.98	0.99	0.93	0.98	0.95	1.00	0.27	0.72

[a] A Gaussian distribution of 15 degrees was assumed as the HEM.
[b] The misorientation between ($\varphi_1=41.46^\circ$, $\phi=70.04^\circ$, $\varphi_2=111.13^\circ$) and the ideal Taylor ($\varphi_1=90.00^\circ$, $\phi=27.00^\circ$, $\varphi_2=45.00^\circ$) is 1.37 degrees.

that the rotation away from the ideal Cube orientation will be faster than for the FC predictions. Based on the rotation rates and the gradient values given in Table 4, FC predicts that the R-Cube texture is metastable in both, plane-strain and equi-biaxial conditions, either at the initial state of deformation or close to failure. To the contrary, the VPSC calculations show the same tendency only in the initial stages of straining, and the difference between both models is only given by the magnitude of the divergence terms. Values for the VPSC model are nearly three times greater than those for the FC calculation. Close to failure, the VPSC computational values show that the R-Cube becomes more stable as it approaches the ideal Taylor orientation in plane-strain, while in balanced-biaxial tension the R-Cube turns in an unstable orientation.

In order to visualize the reorientation tendencies and evolution in Euler space of an individual orientation in the vicinity of the ideal one, typical cross-sections of the rotation field: $\phi-\varphi_1$, $\varphi_2-\varphi_1$, and $\varphi_2-\phi$, were plotted. Each cross-section was evaluated in the range $10^\circ\times10^\circ$ around the selected orientation with a 2° spacing over a regular grid. The arrows specify the directions of orientation change and their lengths indicate the corresponding magnitudes. The absence of arrows in the graphics corresponds to a negligible value of the calculated lattice-rotation rate. At this time, it is important to note two points with respect to the construction of the lattice-rotation field map associated with a deformed state: (i) when the Lagrangian approach is used to describe the texture evolution, orientations initially distributed in the form of a regular grid do not maintain this regularity in the deformed state, (ii) two orientations which are close in the deformed state may come from different initial orientations, which results from different deformation histories, consequently different accumulated shear, critical tensions, etc. can be found. To overcome these problems, we added a fictitious set of orientations (i.e. their associated volume fractions are null) to the ensemble of orientations that described the material texture, in order to evaluate the rotation field at these predefined grid positions. Furthermore, it is necessary to assume that the internal variables associated with these orientations – point charges – have the same microstructural state as the ideal orientation being investigated. In this sense, the calculated rotation-field map is not absolute. The starting orientations have to be specified in the analysis and their validity should be restricted to the vicinity of the orientation studied.

Lattice-rotation field maps for the Cube and R-Cube orientations were calculated, in plane-strain and balanced-biaxial tension at the beginning of deformation and are displayed in Figs. 8a and b and 9a and b, respectively. It can be seen from Fig. 8a that, in the plane-strain condition, orientations around the ideal Cube behave symmetrically with respect to the axes for the three cross-sections analyzed. This characteristic is observed for both FC and VPSC models. The calculated rotation field converges in the φ_1 direction and diverges away from it in the ϕ direction, while a negligible rotation occurs along the φ_2 axis, particularly those orientations very close to the ideal Cube. Both schemes predict a flow of the rotation field that tends to move away in the direction of ϕ (i.e. towards the Goss orientation). Orientations rotate slowly during this process; however the predicted magnitudes of the lattice-rotation rates are stronger for the VPSC than for the FC model. In balanced-biaxial loading, the flow around the Cube orientation is a two-dimensional divergent in the ϕ,φ_2 directions; the term $\partial\dot{\varphi}_1/\partial\varphi_1$ is null and no rotation occurs along this axis. This effect can be clearly seen in the $\varphi_2-\phi$ section (Fig. 8b). Again, the changes in the magnitudes are rather small in the FC calculations.

Results based on the rotation rates and gradient values indicate that the R-Cube orientations are metastable in both, the plane-strain and the balanced-biaxial conditions. This is shown in Table 4 and depicted in Fig. 9a and b. It can be seen in Fig. 9a that, during plane-strain deformation, a three-dimensional divergence is present in the rotation field around the ideal R-Cube. Computations indicate that both schemes predict the same behavior; however, as shown for the Cube case, the magnitudes are nearly three times larger for the VPSC calculations. As a consequence, a surprisingly large reduction in the intensity of this component occurs. The main lattice rotation takes place in the directions ϕ,φ_2, towards the Taylor orientation, and only a weak divergence is observed along the diagonal line; this can be more easily seen in the $\varphi_2-\phi$ section. The values simulated for equi-biaxial stretching and plotted in Fig. 9b indicate that there is no rotation along the φ_1 axis. The farther an orientation is from the ideal position, the higher its rotation rate is in the ϕ,φ_2 directions. The two-dimensional divergence of rotation observed for balanced-biaxial loading is seen in both Cube and R-Cube orientations, and it is entirely attributed to the symmetry of the test.

Fig. 10 shows the initial and final (at the limit-strain level) inverse pole figures for the Cube and R-Cube textured materials for plane-strain and equi-biaxial stretching. The inverse pole figures predicted at failure by both models are in close agreement with

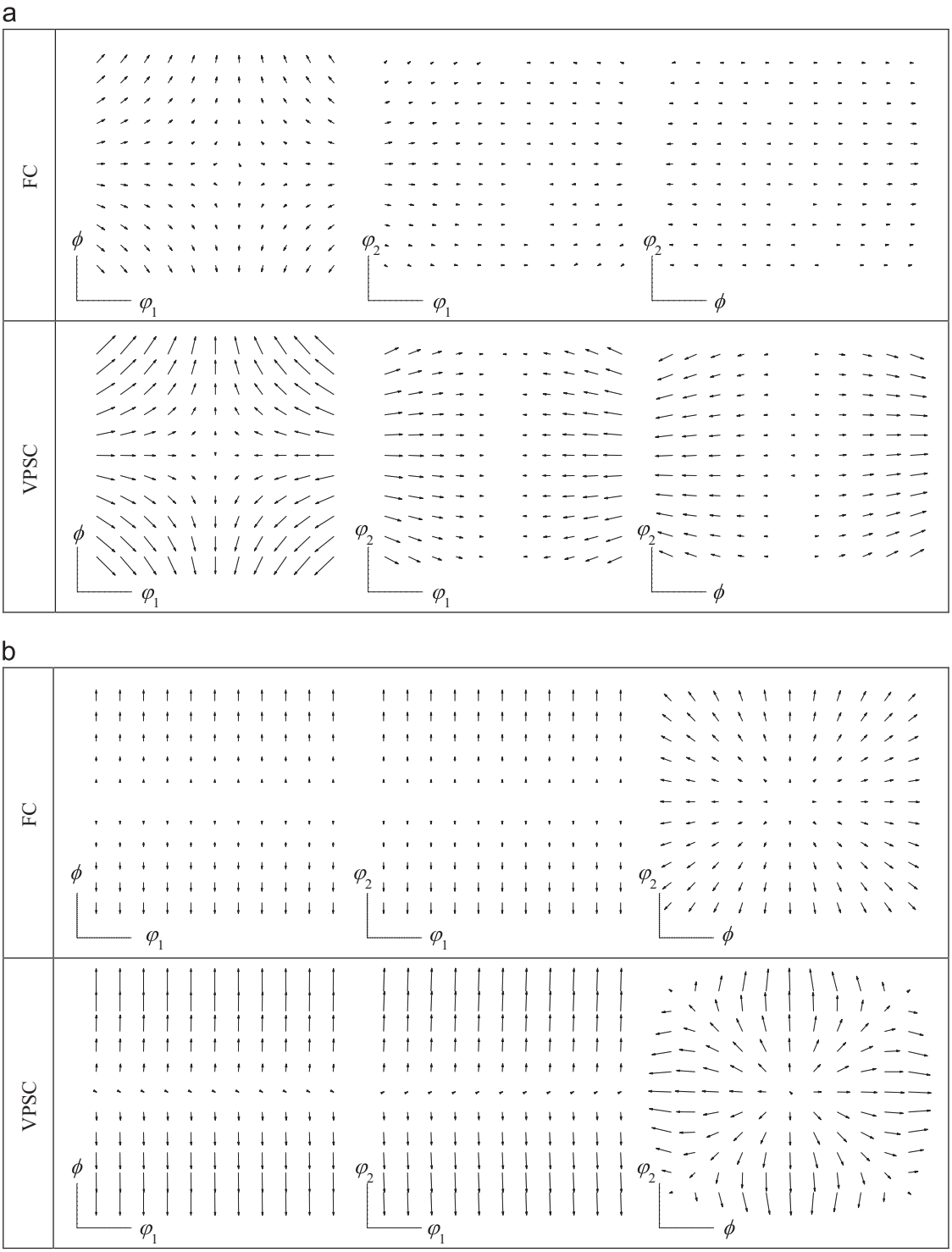

Fig. 8. (a) Lattice rotation-field map for the Cube orientation ($\varphi_1 = 0^\circ$, $\phi = 90^\circ$, $\varphi_2 = 90^\circ$) in the plane-strain stretching predicted by the FC and VPSC models (multiplier magnitude = 100). (b) Lattice rotation-field map for the Cube orientation ($\varphi_1 = 0^\circ$, $\phi = 90^\circ$, $\varphi_2 = 90^\circ$) in equi-biaxial deformation state predicted by the FC and VPSC models (multiplier magnitude = 50).

one another for the Cube material in plane-strain tension. As biaxial stretching proceeds, differences appear, and in balanced-biaxial stretching, the behavior of certain crystallographic orientations depends on the interaction model used. Particularly, near the ⟨001⟩ orientations, results of the models diverge. Using the VPSC approach, only a few orientations remain close to ⟨100⟩, but for the FC simulations this is not the case, and the grains rotate in widely different directions. In both cases, one can trace an imaginary line that delineates a zone with a high density of orientations and one vacant of orientations. The grain orientations tend to rotate and accumulate in the region approximately defined by ⟨115⟩−⟨114⟩ and ⟨104⟩−⟨102⟩ for FC and by ⟨116⟩−⟨115⟩ and ⟨104⟩−⟨305⟩ for VPSC, respectively. In addition, we found that the FC final orientations are distributed rather uniformly in the inhabited region. Interestingly, for the VPSC calculations, there is a preference to rotate halfway up the ⟨105⟩−⟨304⟩ segment line. As expected, due to the symmetry of the test, almost the same behavior is observed for the initial R-Cube textured-material in balanced-biaxial loading.

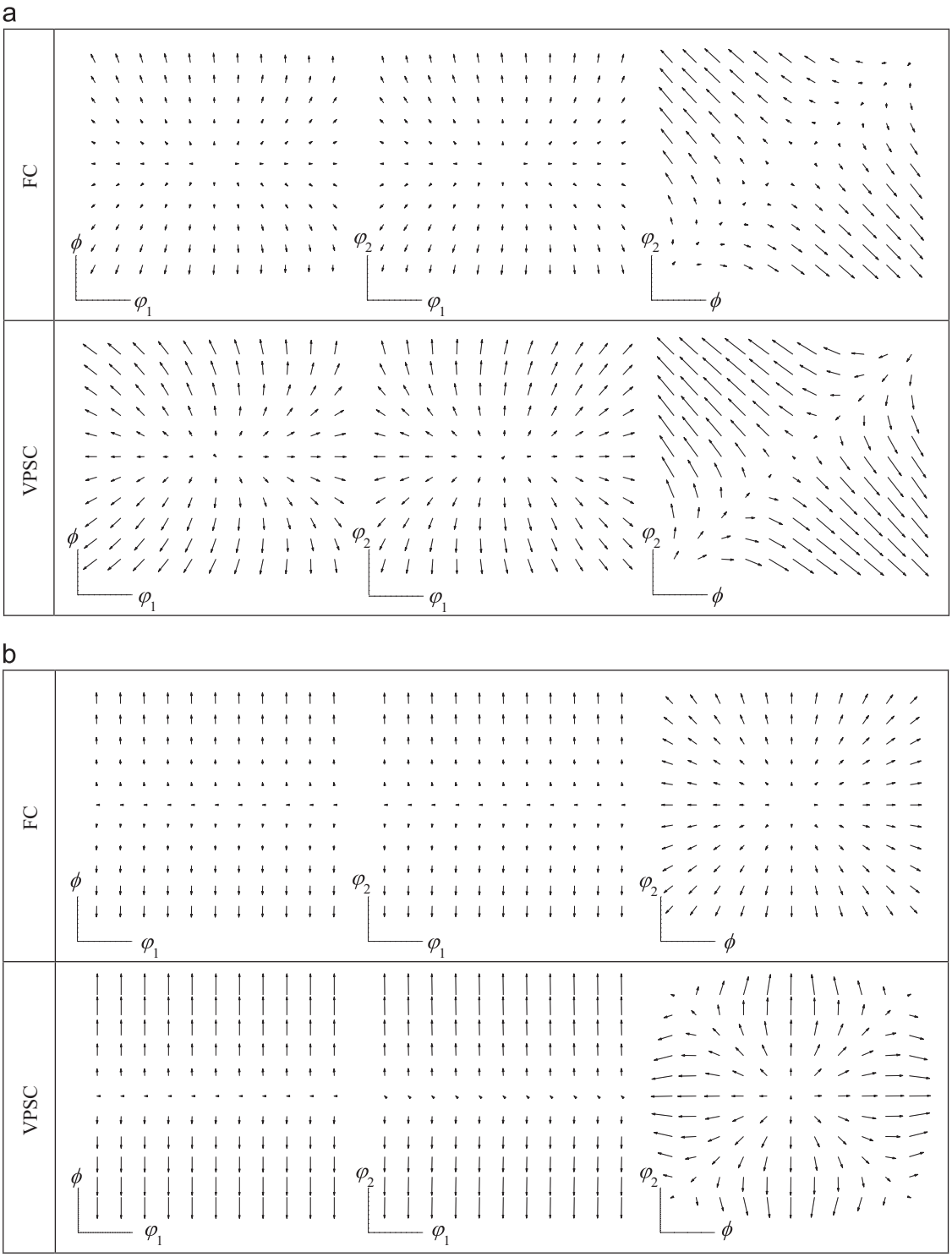

Fig. 9. (a) Lattice rotation-field map for the R-Cube orientation ($\varphi_1=45^\circ$, $\phi=90^\circ$, $\varphi_2=90^\circ$) in plane-strain stretching predicted by the FC and VPSC models (multiplier magnitude=50). (b) Lattice rotation-field map for R-Cube orientation ($\varphi_1=45^\circ$, $\phi=90^\circ$, $\varphi_2=90^\circ$) in equi-biaxial deformation state predicted by the FC and VPSC models (multiplier magnitude=50).

Just less than ten ($<1\%$) orientations very close to ⟨001⟩ show a slight difference in their final orientations. The main discrepancies between models take place for the R-Cube in plane-strain stretching. As deformation proceeds, the initial R-Cube orientations move progressively to more stable positions S ($\varphi_1=59^\circ$, $\phi=37^\circ$, $\varphi_2=63^\circ$), Copper ($\varphi_1=90^\circ$, $\phi=35^\circ$, $\varphi_2=45^\circ$) and Taylor ($\varphi_1=90^\circ$, $\phi=27^\circ$, $\varphi_2=45^\circ$). The speed with which this happens creates the difference between the two models' predictions. At failure, VPSC has 75% of Copper and Taylor, 10% of S and no R-Cube orientations present, while the FC calculation retains an appreciable 20% of R-Cube and no Copper is obtained.

As mentioned above, two orientations that share a similar position in Euler space in the deformed material may come from different initial orientations, and consequently, present distinct deformation histories. In what follows, we will discuss the evolution of two typical orientations, one near R-Cube (#1 $\varphi_1=99.18^\circ$,

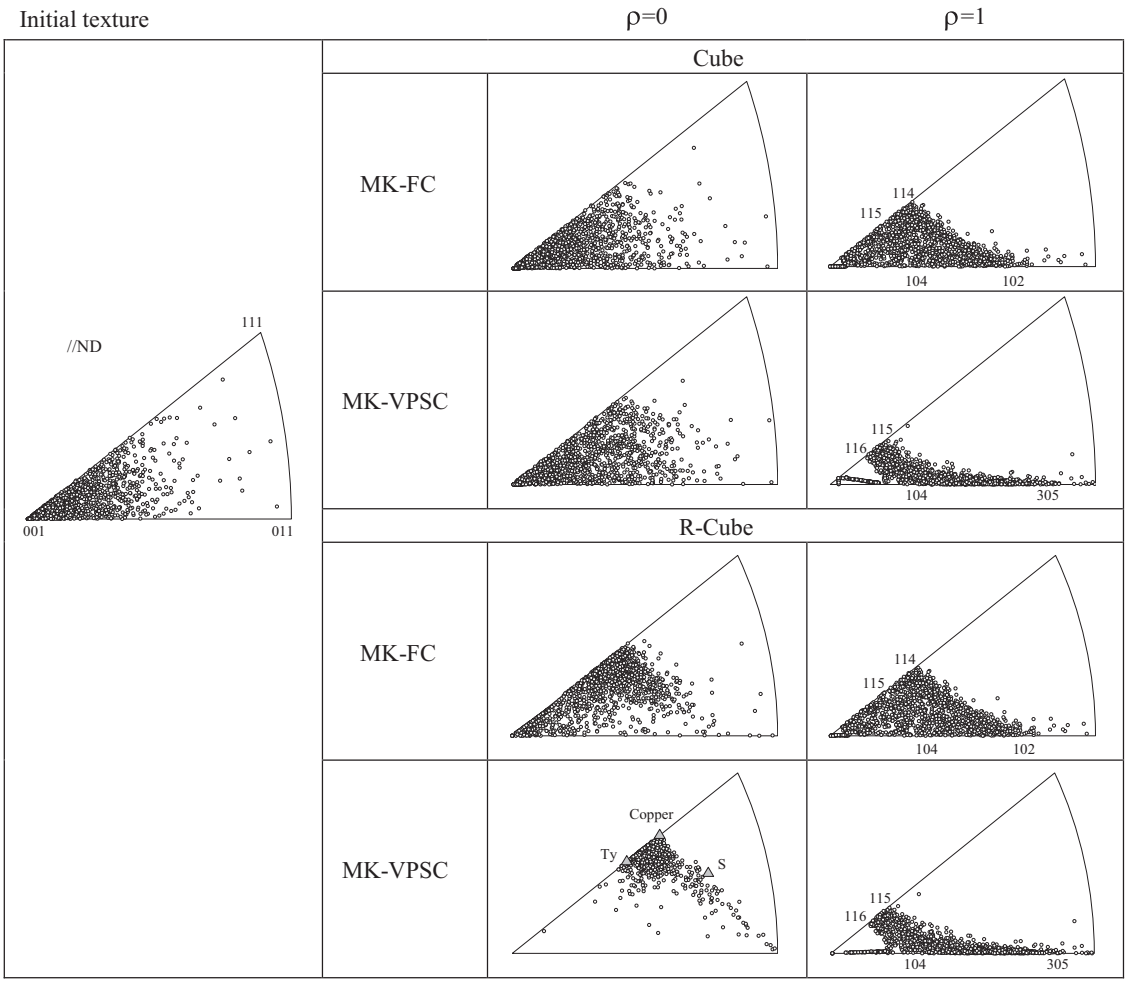

Fig. 10. Equal-area inverse pole figures showing the initial (left) and predicted final (right) orientations at failure calculated with MK-FC and MK-VPSC models for the Cube and R-Cube textured materials.

$\phi = 3.94^\circ$, $\varphi_2 = -54.08^\circ$) and the other close to the Taylor component (#2 $\varphi_1 = -90.24^\circ$, $\phi = 26.84^\circ$, $\varphi_2 = 139.22^\circ$). At failure, both are very close to the ideal Taylor orientation. As seen in Fig. 11b, the first one undergoes a significant reorientation, and rotates towards the more stable Taylor orientation; this behavior is also observed using the FC model, but the reorientation process is slower. The persistence values change from 0.16 to 0.33 and from 0.21 to 0.60 for orientations #1 and #2, respectively, and the calculated rotation fields (Fig. 11a and d) are in agreement with the observed evolution of the Euler angles (Fig. 11b and e). In addition, the almost one-dimensional convergence is compatible with the dispersion observed in Fig. 11c and f. These pole figures display what would happen if a fictitious set of orientations with an initial dispersion of 3° is used to understand how individual orientations evolve with increasing strain.

The texture evolution during rolling of a polycrystalline aluminum alloy with initial Cube and R-Cube textures was experimentally investigated by Liu et al. [46] and Liu and Morris [47]. For the case of the initial Cube texture, the experimental results show that the Cube-oriented grains rotated to the β-fiber along different paths, leading to an increase of the intensity at the Copper and Taylor orientations. For the R-Cube texture, they found that grains with the {001} ⟨110⟩ orientation are unstable, and during rolling, they gradually rotate towards Copper and Taylor with a pronounced scattering towards S. As the cold-rolling reduction increases, the intensity of the R-Cube orientation decreases, while the intensity of orientations shared by Copper and Taylor increases. When the cold-rolling reduction reaches about 64%, the intensity of R-Cube decreases to zero. VPSC predictions in plane strain are fully consistent with Liu and Morris' measurements.

Finally, in order to complete the present analysis, we plot the evolution of some of the ideal texture components during the deformation process. In particular, we are interested in those orientations predicted at failure. Fig. 12 shows a reorientation towards the more stable positions of the initial Cube and R-Cube textured materials, for plane-strain and equi-biaxial stretching. Qualitatively, both models behave similarly for the main texture components, but differ in the velocity with which the process takes place, as was discussed previously. Tadano et al. [48] recently highlighted similar results that show the relation between texture intensity and a sharper lattice-rotation field for the case of a Cube-type texture treated within the FC or homogenization-based, finite-element-method framework. The Cube texture shows the minor differences between both models in plane-strain loading (Fig. 12a). However, in equi-biaxial stretching, VPSC shows a faster reduction of the initial Cube orientations than FC. It is interesting to note that the volume fraction of the Cube orientations is similar for both cases at failure, around 35–40% (Fig. 12b). Also, the R-Cube exhibits identical behavior in equi-biaxial stretching (Fig. 12d). The main differences in magnitude appear for R-Cube in plane-strain (Fig. 12c). At the beginning of the deformation process, both FC and VPSC predict similar texture evolution, but as deformation proceeds quantitative and qualitative changes in the evolution

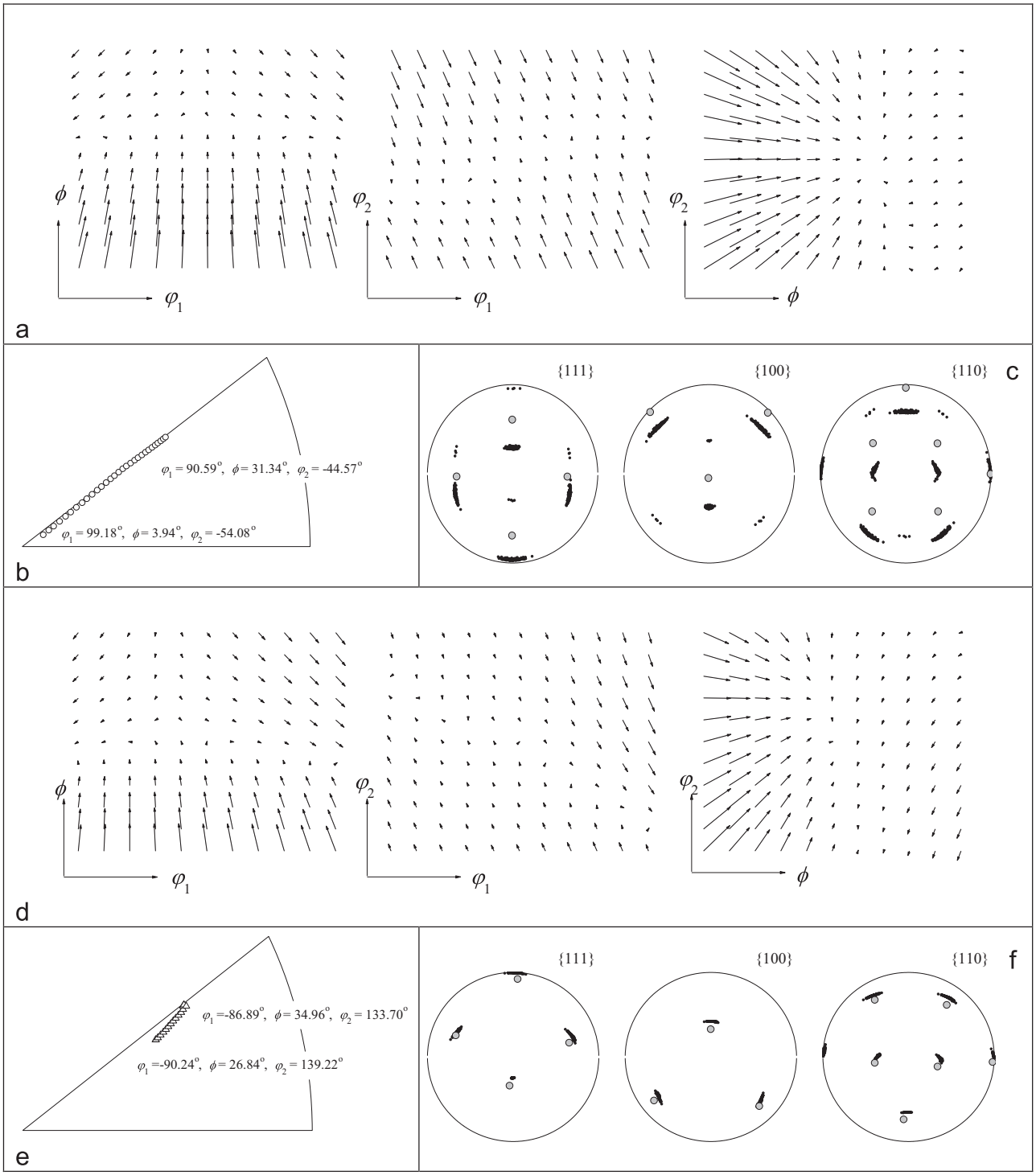

Fig. 11. VPSC's predictions during plane-strain drawing. Starting orientation (a and c) near R-Cube and (d and f) near Taylor. (a and d) Cross-sections of the lattice-rotation field at failure (multiplier magnitude = 50). (b and e) Inverse pole figures displaying the rotation path followed during the deformation process. (c and f) Final distribution of orientations caused by an initial dispersion of 3°. Initial orientations are in shaded grey.

profile are observed, in particular as the limit-strain values are approached. Near the failure strain, no R-Cube orientations are present in the VPSC simulated texture, while the FC calculation maintains nearly one third of the initial R-Cube orientations. A decomposition of the crystal orientations indicates that the reorientation towards the two complementary Copper-Taylor components is faster in VPSC than in FC calculations, and these components constitute about 60% and 70% of the orientations at failure for VPSC and FC models, respectively. The same tendency is observed for the S orientations, but their intensities are lower by an order of magnitude.

The final orientations depend on the imposed strain path and the selected model. This suggests that the way in which the initial textures evolve is the key to interpret the limit-strain profiles. In what follows, we evaluate the relation between orientation stability and geometrical hardening due to grain rotations, as well as how stability and hardening affect the predicted and enhanced forming-limit strains.

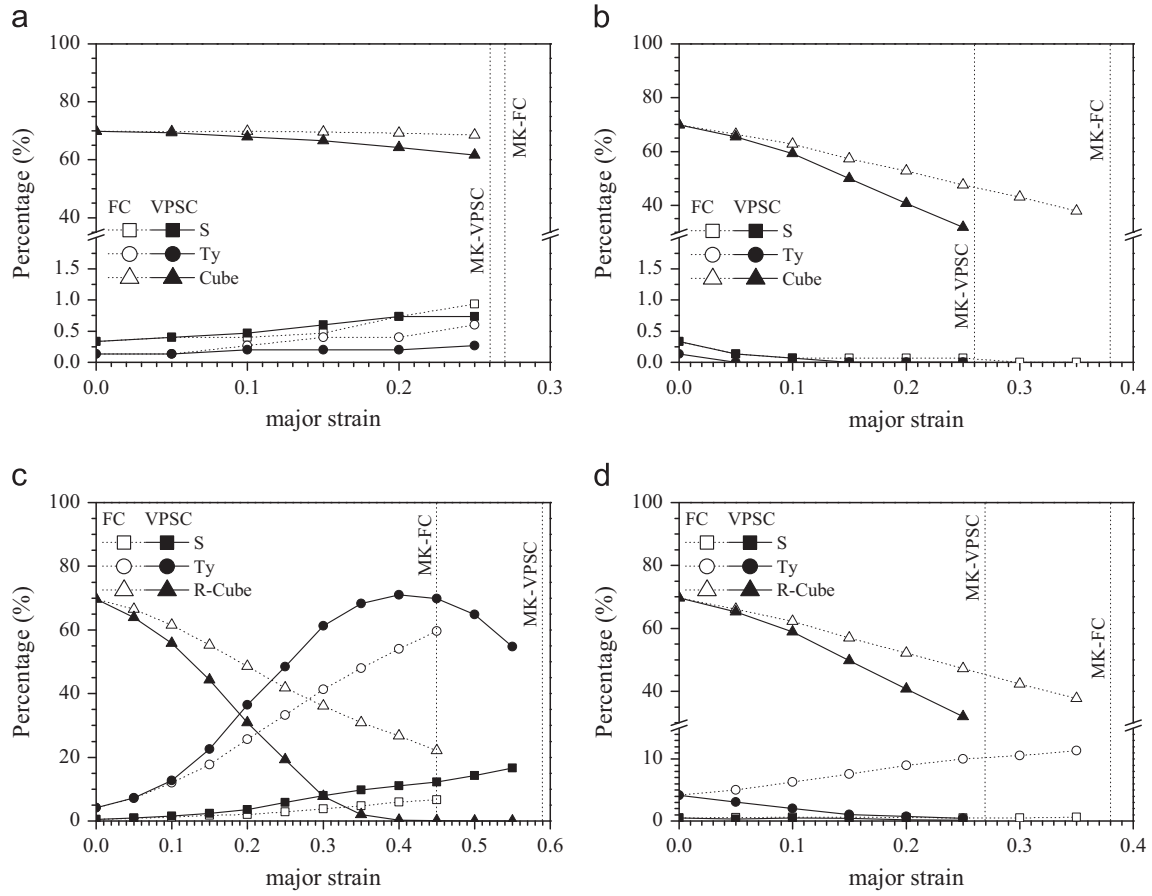

Fig. 12. Evolution of the ideal-texture components in plane-strain and equi-biaxial stretching for Cube and R-Cube. The ideal components were calculated with a tolerance spread of 15°. (a) Cube. Plane-strain, (b) Cube. Equi-biaxial, (c) R-Cube. Plane-strain and (d) R-Cube. Equi-biaxial.

4. Geometrical hardening

Miller and Dawson [49] pointed out that both material and geometrical hardening elevate the flow stress during straining. Dislocation interactions increase the slip resistance, and hence the macroscopic flow stress. This is known as material hardening. In addition, as plastic deformation proceeds, the grains rotate changing the orientations of each slip system, which results is an increase or decrease in the macroscopic flow stress required for continuous plastic deformation. This effect is referred to as geometrical (textural) hardening or softening. Yoshida et al. [11] numerically investigated the geometrical hardening/softening effect for textured aluminum-alloy sheets in the plane-strain stretching mode using a generalized FC Taylor-type polycrystalline model. Based on these calculations, they proposed that geometrical hardening effectively develops high-formability in sheet metals. To rank the relative importance of the development of anisotropy during straining (geometrical hardening) versus the effects of the initial grain distributions, we repeated the calculations of the limit-strain values but without texture evolution. Results for plane-strain deformation, calculated using both models (MK-FC and MK-VPSC) are presented in Table 5. We confirm that texture evolution promotes high formability, not the particular initial texture we considered. When texture is not updated, the calculated limit strains are nearly identical – between 0.26 and 0.28 – irrespective of the computational model or initial orientation. These results point out the importance of the stability analysis conducted in the previous section.

It is evident that geometrical hardening takes place for the R-Cube and the ND-Cube cases, while no effect is observed for the

Table 5
Calculated plane-strain limit values, with and without texture evolution, beginning with Cube, R-Cube and ND-Cube textured materials.

	Cube		R-Cube		ND-Cube	
	with	without	with	without	with	without
MK-FC	0.28	0.28	0.47	0.28	0.34	0.28
MK-VPSC	0.27	0.27	0.59	0.27	0.38	0.26

Cube texture. Moreover, the greatest influence of geometrical hardening is predicted when the VPSC scheme is used, particularly for the R-Cube texture, where the major limit strain is 1.3 times greater than for the FC calculation. The difference between models can be understood by analyzing the geometrical flow stress (i.e. calculations are carried out assuming that material hardening does not occur). The amount of strain nearly corresponds to the necking limit strains. The predicted stress-strain relations are displayed in Fig. 13, where the macroscopic flow stress σ_{11} is normalized by $\sigma_{11(0)}$, which is the value of σ_{11} at $\varepsilon_{11}=0$. The enhanced-formability tendency due to the geometrical hardening reported in Yoshida's work is also observed with the VPSC scheme. Thus, it can be clearly seen that the polycrystal-plasticity scheme substantially affects the geometrical hardening, and therefore, the FLD values.

As was shown in Section 3, only a very small amount of texture evolution is observed when the Cube texture is deformed, regardless of the model. At small deformations, $\varepsilon_{11}<0.1$, grain rotations have a limited influence on the flow curve for R-Cube and ND-Cube textures – using either FC or VPSC schemes – but from this

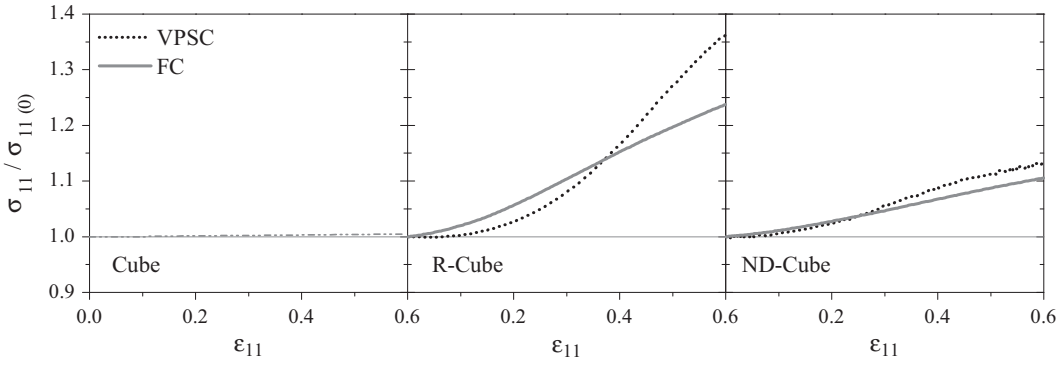

Fig. 13. Normalized stress–strain curves in the plane-strain stretching mode.

Table 6
Calculated limit-strain values, with and without texture evolution, in balanced-biaxial mode around the Cube, R-Cube and ND-Cube textured materials.

	Cube		R-Cube		ND-Cube	
	with	without	with	without	with	without
MK-FC	0.38	0.21	0.38	0.21	0.47	0.34
MK-VPSC	0.26	0.16	0.26	0.16	0.26	0.18

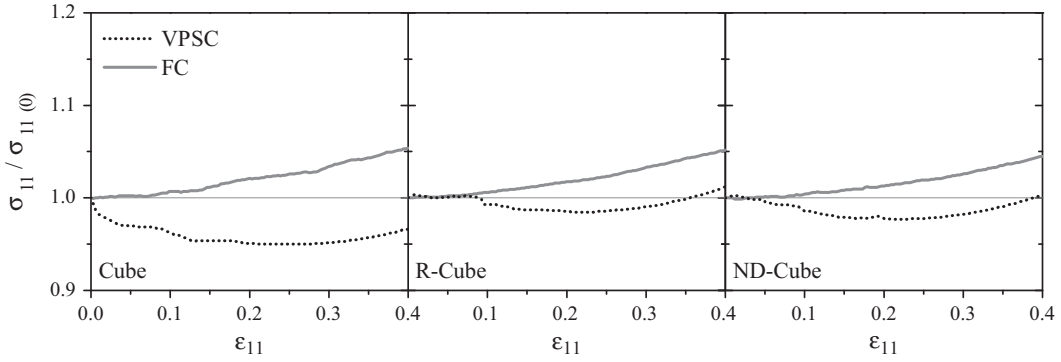

Fig. 14. Normalized stress–strain curves in equi-biaxial stretching.

value the geometrical hardening has a non-negligible contribution. As deformation progresses, the differences between models are reflected in the slope of the plots, particularly for R-Cube. At the beginning of deformation the normalized VPSC stress–strain curve increases in slope up to a strain at approximately $\varepsilon_{11}=0.30$, but from this point the rate remains constant. To the contrary, when FC scheme is used, the geometrical hardening exhibits a uniform slope over the entire deformation range. The resulting normalized flow curve is greater than for the VPSC model up to $\varepsilon_{11}=0.38$, but from that point on the situation reverses and VPSC predicts a pronouncedly higher normalized flow stress. This response delays the occurrence of localized necking through a continuous positive change of the hardening rate, and therefore, the limit-strain values are higher in the VPSC simulations. Minor differences are found between both approaches for ND-Cube, although the same behavior is observed, the higher the geometrical hardening, the higher the limit-strain value.

The lack of geometrical hardening predicted for the Cube material is a consequence of its stability, which are characterized in Table 3. The divergence is zero and almost null for FC and VPSC respectively, while the persistence value remains close to its maximum. As mentioned above, these orientations rotate slowly during plane-strain deformation, as the rotation fields converge in one direction but diverge away from one another in the others. In contrast to the flow around Cube, significant geometrical hardening is observed around the R-Cube orientation. This fact is closely associated with the stability parameters calculated for the initial state of deformation. A three-dimensional divergence occurs, since all the gradients are positive, as shown in Table 4. Besides, the persistence parameters for both schemes are lower than those of Cube. The large differences in the predicted stability parameters correlate well with the different profiles displayed in Fig. 13.

To the authors' knowledge, all results relating geometrical hardening to the limit strains that are reported in the literature focus on the plane-strain stretching mode. Therefore, we investigated if this relation holds for other strain paths; in particular, we concentrated on the balanced-biaxial mode. In the same manner as done for plane-strain stretching, the limit strains for $\rho=1$ were recalculated but without allowing texture evolution (see Table 6). The decrease of the predicted limit strains is verified, sharing the tendency observed from the plane-strain analysis. For both models due to the test symmetry, the Cube and R-Cube materials have equal limit values, within numerical differences. Without texture

evolution, MK-VPSC predicts a tendency towards equilibration of the limit-strain values, similar to that observed in plane-strain. It is interesting to note that when texture evolution is omitted in MK-FC, the calculated ND-Cube limit strain does not decrease sufficiently to conclude that the remaining difference is independent of the calculation model. As was seen in Table 5 and Fig. 13, the increase in formability under plane-strain conditions shows a high correlation with the predicted geometrical hardening. However, an opposite geometrical contribution is predicted in balanced-biaxial loading. FC promotes geometrical hardening, while VPSC lead to a geometrical softening. The normalized stress–strain curves are displayed in Fig. 14. It is observed that the FC geometrical hardening increases continuously at a nearly constant rate with deformation. While, in the case of the VPSC calculation the maximum geometrical-softening contribution occurs close to the failure strain. Finally, regarding Table 6 and Fig. 14, it is not possible to conclude that there is a clear correlation between geometrical hardening/softening and the limit strain in biaxial stretching. The greater formability predicted by MK-FC does not directly correspond to just the associated textural hardening, but it also exhibits the effects of the interaction model used.

5. Conclusions

In the present study, the role of the constitutive model in the forming limit of FCC sheet metals with Cube, R-Cube and ND-Cube type material textures was investigated. The enhanced formability predicted for the R-Cube material close to a plane-strain loading mode was explained in terms of stability and geometrical hardening. The following remarks summarize this work and describe our conclusions:

- The classical MK model, based on strain-rate imposed boundary conditions, was generalized in order to explicitly include stress loading conditions. With the goal of comparing our predictions to experimental data, all the components of the stress tensor were assumed zero except that in the loading direction. To accomplish this, the velocity-gradient tensor components $\bar{L}_{22}$ and $\bar{L}_{33}$ were adjusted in order to nullify the corresponding stresses components. This allowed us to account for the evolution of anisotropy during the test.
- Quantitatively and qualitatively different predictions are obtained when using either MK-FC or MK-VPSC models in the uniaxial and balanced-biaxial stretching. In negative strain space both models predict similar shapes for the FLD curve for the Cube and ND-Cube textured materials, although the calculated values are lower for the FC simulations. The behavior is quite different for R-Cube, since the FC's predicted curve slopes downwards from plane-strain to uniaxial stretching with the minimum limit-strain value at $\rho=-0.5$. The opposite is found using MK-VPSC. Nevertheless, the limit strains predicted by both models are close for R-Cube when strictly uniaxial tensile conditions are imposed.
- The rotation rates, their gradients and divergences at and around the individual orientations were used to examine the stability of the ideal Cube and R-Cube textures, during plane-strain and equi-biaxial stretching. As expected, negligible rotation rates are predicted for the ideal Cube orientation independent of the selected model. However, the VPSC orientation gradient is higher than that for FC, implying that its rotation rate will be faster than that predicted with the FC model in the vicinity of the ideal orientation. This behavior is also observed for the R-Cube orientation, although this texture has a more pronounced metastable tendency (i.e. higher divergency value). As a consequence, a remarkable reduction in the intensity of this component occurs.
- The higher formability exhibited by the R-Cube and ND-Cube materials in the plane-strain deformation mode is directly related to the geometrical hardening predicted by both FC and VPSC schemes. Moreover, the greatest influence is found when the VPSC model is used, particularly for the R-Cube texture. Although we studied three different textures, it is texture evolution, and not the particular initial textures considered here that promotes high formability. The lack of geometrical hardening predicted for the Cube texture is a consequence of the slow rotation of orientations during plane-strain deformation, as demonstrated by the calculated stability parameters.
- The loss of formability predicted by MK-VPSC in balanced-biaxial stretching for the three textured-materials is directly associated to the predicted geometrical softening. To the contrary, the high formability predicted by MK-FC for the ND-Cube material is not only correlated with geometrical or textural hardening, but also with the interaction model used.

Acknowledgments

This research was supported by the CONICET (Consejo Nacional de Investigaciones Científicas y Técnicas) PIP-11220100100257 and by the ANPCyT PICT-1341. The authors wish to acknowledge M.G. Stout for fruitful comments about the present manuscript.

Appendix A. Supplementary material

Supplementary data associated with this article can be found in the online version at http://dx.doi.org/10.1016/j.ijmecsci.2014.05.031.

References

[1] Grewen J, Huber J. Recrystallization of metallic materials. In: Riederer F Haessner, editor. Stuttgart; 1978. p. 111–36.
[2] Duckham A, Engler O, Knutsen RD. Moderation of the recrystallization texture by nucleation at copper-type shear bands in Al–1Mg. Acta Mater 2002;50:2881–93.
[3] Crumbach M, Goerdeler M, Gottstein G. Modelling of recrystallisation textures in aluminium alloys: II. Model performance and experimental validation. Acta Mater 2006;54:3291–306.
[4] Choi S-H, Brem JC, Barlat F, Oh KH. Macroscopic anisotropy in AA5019A sheets. Acta Mater 2000;48:1853–63.
[5] Lopes AB, Barlat F, Gracio JJ, Ferreira Duarte JF, Rauch EF. Effect of texture and microstructure on strain hardening anisotropy for aluminum deformed in uniaxial tension and simple shear. Int J Plast 2003;19:1–22.
[6] Yoon JW, Barlat F, Gracio JJ, Rauch EF. Anisotropic strain hardening behavior in simple shear for cube textured aluminum alloy sheets. Int J Plast 2005;21:2426–47.
[7] Chiba R, Takeuchi H, Kuroda M, Hakoyama T, Kuwabara T. Theoretical and experimental study of forming-limit strain of half-hard AA1100 aluminium alloy sheet. Comput Mater Sci 2013;77:61–71.
[8] Yanaga D, Kuwabara T, Uema N, Asano M. Material modeling of 6000 series aluminum alloy sheets with different density cube textures and effect on the accuracy of finite element simulation. Solids Struct 2012;49:3488–95.
[9] Wu PD, Mac Ewen SR, Lloyd DJ, Neale KW. Effect of cube texture on sheet metal formability. Mater Sci Eng A 2004;364:182–7.
[10] Yoshida K, Ishizaka T, Kuroda M, Ikawa S. The effects of texture on formability of aluminum alloy sheets. Acta Mater 2007;55:4499–506.
[11] Yoshida K, Tadano K, Kuroda M. Improvement in formability of aluminum alloy sheet by enhancing geometrical hardening. Comput Mat Sci 2009;46:459–68.
[12] Marciniak Z, Kuczynski K. Limit strains in the process of stretch-forming sheet metal. Int J Mech Sci 1967;9:609–20.
[13] Signorelli JW, Bertinetti MA. On the role of constitutive model in the forming limit of FCC sheet metal with cube orientations. Int J Mech Sci 2009;51:473–80.

[14] Yoshida K, Kuroda M. Numerical investigation on a key factor in superior stretchability of face-centered cubic polycrystalline sheets. Int J Mech Sci 2012;58:47–56.
[15] Kocks UF, Tomé CN, Wenk H-R. Texture and anisotropy: preferred orientations in polycrystals and their effect on materials properties. UK: Cambridge University Press; 052179420X (ISBN: 9780521794206).
[16] Roters F, Eisenlohr P, Hantcherli L, Tjahjanto D, Bieler T, Raabe D. Overview of constitutive laws, kinematics, homogenization and multiscale methods in crystal plasticity finite-element modeling: theory, experiments, applications. Acta Mater 2010;58:1152–211.
[17] Lee EH. Elastic–plastic deformation at finite strains. Appl Mech 1969;36:1–14.
[18] Teodosiu, C. A dynamic theory of dislocations and its applications to the theory of the elastic-plastic continuum. In: Simmons, J.A., de Witt, R., Bullough, R., (Eds.), Fundamental Aspects of Dislocation Theory, Nat. Bur. Stand. (U.S.), Spec. Publ. 317, II, 1970, pp. 837–876.
[19] Hutchinson J.W. Bound and self-consistent estimated for creep of polycrystalline materials. In: Proceedings of the Royal Society London A; 1976 348: p. 101–27.
[20] Molinari A, Canova GR, Ahzi S. A self-consistent approach of the large deformation polycrystal viscoplasticity. Acta Metall 1987;35:2983–94.
[21] Lebensohn RA, Tome CN. A self-consistent approach for the simulation of plastic deformation and texture development of polycrystals: application to Zr alloys. Acta Metall Mater 1993;41:2611–24.
[22] Mura T. Micromechanics of defects in solids. Dordrecht, The Netherlands: Martinus Nijhoff Publishers; 1987.
[23] Wu PD, Mac Ewen SR, Lloyd DJ, Neale KW. A mesoscopic approach for predicting sheet metal formability. Model Simul Mater Sci Eng 2004;12:511–27.
[24] Wang H, Wu PD, Boyle KP, Neale KW. On crystal plasticity formability analysis for magnesium alloy sheets. Int J Solids Struct 2011;48:1000–10.
[25] Hutchinson JW, Neale KW. Sheet necking II: time-independent behavior. In: Koistinen DP, Wang NM, editors. Mechanics of sheet metal forming. New York-London: Plenum Press; 1978. p. 127–53.
[26] Wu P.D., Neale K.W., Van der Giessen E. On crystal plasticity FLD analysis. In: Proceedings of the Royal Society London A; 1997 453: p. 1831–1848.
[27] Kuroda M, Tveergard V. Forming limit diagrams for anisotropic metal sheets with different yield criteria. Int J Solids Struct 2000;37:5037–59.
[28] Signorelli JW, Bertinetti MA, Turner PA. Predictions of forming limit diagrams using a rate-dependent polycrystal self-consistent plasticity model. Int J Plast 2009;25:1–25.
[29] Serenelli MJ, Bertinetti MA, Signorelli JW. Investigation of the dislocation slip assumption on formability of BCC sheet metals. Int J Mech Sci 2010;52:1723–34.
[30] Serenelli MJ, Bertinetti MA, Signorelli JW. Study of limit strains for FCC and BCC sheet metal using polycrystal plasticity. Int J Solids Struct 2011;48:1109–19.
[31] Signorelli JW, Serenelli MJ, Bertinetti MA. Experimental and numerical study of the role of crystallographic texture on the formability of an electro-galvanized steel sheet. J Mater Process Technol 2012;212:1367–76.
[32] Zhou Y, Neale KW. Predictions of forming limit diagrams using a rate-sensitive crystal plasticity model. Int J Mech Sci 1995;37:1–20.
[33] Tóth L, Neale KW, Jonas JJ. Stress response and persistence characteristics of the ideal orientations of shear textures. Acta Metall 1989;37:2197–210.
[34] Clement A, Coulomb P. Eulerian simulation of deformation textures. Scr Metall 1979;13:899–901.
[35] Beausir B, Tóth L, Neale KW. Ideal orientations and persistence characteristics of hexagonal close packed crystals in simple shear. Acta Mater 2007;55: 2695–705.
[36] Arzhagui M, Beausir B, Tóth L. Contribution of non-octaedral slip to texture evolution of fcc polycrystals in simple shear. Acta Mater 2009;57:2440–53.
[37] Pandey A, Khan A, Kim E-Y, Choi S-H, Gnäupel-Herold T. Experimental and numerical investigations of yield surface, texture, and deformation mechanisms in AA5754 over low to high temperatures and strain rates. Int J Plast 2012;41:165–88.
[38] Li F, Bate PS. Strain path change effects in cube texture aluminium sheet. Acta Metall Mater 1991;39:2639–50.
[39] Ryen Øyvind. Work hardening and mechanical anisotropy of aluminium sheets and profiles [Ph.D. thesis]. Norwegian University of Science and Technology (NTNU); 2003.
[40] Moy C, Weiss M, Xia J, Sha G, Ringer S. Influence of heat treatment on the microstructure, texture and formability of 2024 aluminium alloy. Mater Sci Eng A 2012;552:48–60.
[41] Tajally M, Emadoddin E. mechanical and anisotropic behavior of 7075 aluminum alloy sheets. Mater Des 2011;32:1594–9.
[42] Lademo O, Pedersen K, Berstad T, Furu T, Hopperstad O. An experimetnal and numerical study on the formability of textured AlZnMg alloys. Eur J Mech A/Solids 2008;27:116–40.
[43] Velmanirajan K, Anuradha K, Thaheer S, Narayanasamy R, Madhavan R, Suwas S. Experimental investigation of forming limit, void coalescence and crystallographic textures of aluminum alloy 8011 sheet annealed at various temperatures. Arch Civil Mech Eng 2013.
[44] Pedersen K, Lademo O, Berstad T, Furu T, Hopperstad O. influence of texture and grain structure on strain localisation and formability for AlMgSi alloys. J Mater Process Technol 2008;200:77–93.
[45] Zhou Y, Neale KW. Influence of FCC rolling textures on biaxial sheet stretching. Acta Metall Mater 1994;42:2175–89.
[46] Liu WC, Man C-S, Morris JG. Lattice rotation of the cube orientation to the β fiber during cold rolling of AA 5052 aluminum alloy. Scr Mater 2001;45:807–14.
[47] Liu WC, Morris JG. texture evolution of polycrystalline AA 5182 aluminum alloy with an initial {001} ⟨110⟩ texture during rolling. Scr Mater 2002;47:487–92.
[48] Tadano Y, Kuroda M, Noguchi H. Quantitative re-examination of Taylor model for FCC polycrystals. Comput Mater Sci 2012;51:290–302.
[49] Miller M, Dawson P. Influence of slip system hardening assumptions on modeling stress dependence of work hardening. J Mech Phys Solids 1997;45:1781–804.